Occurrence of rare lightning events during Hurricane Nicholas (2021)

Timothy Logan[1*], Jacob Hale[1], Sydney Butler[1], Brendan Lawrence[1], and Samuel Gardner[2]

[1] Texas A&M University, College Station, Texas

[2] Texas Tech University, Lubbock, Texas

Submitted to *Journal of Geophysical Research-Atmospheres*

Corresponding author address: Dr. Timothy Logan, the Department of Atmospheric Sciences, Texas A&M University, 3150 TAMU, College Station, TX 77843-3150. Email: tlogan52@tamu.edu, 979-845-2004.

Abstract

Hurricane Nicholas was classified as a Category 1 tropical cyclone (TC) at 0000 UTC on 14 September 2021 and made landfall along the upper Texas Gulf Coast at 0530 UTC with maximum sustained winds of 33 m s^{-1}. Much of the electrical activity during Nicholas was monitored by the Houston Lightning Mapping Array (HLMA) network. Deep convection developed in the rainband at 1700 UTC on 13 September, diminished by 2030 UTC, and re-intensified after 2200 UTC. At 2004 UTC (13 September), a curved megaflash (~220 km) was observed by the HLMA in the stratiform precipitation region of the outer rainband. By 0130 UTC on 14 September 2021, vigorous deep convective cells developed in the eastern eyewall region and propagated cyclonically to the western eyewall region. Several "jet-like" transient luminous events (TLEs) were observed by the HLMA emanating from a deep convective cell in the western eyewall region between 0230-0300 UTC with VHF source points ranging from 30-45 km in altitude. Moreover, the TLEs occurred within a region of strong wind shear, upper-level graupel-ice crystal collisions (~15 km), and strong cloud top divergence. Charge analysis of the deep convection during Nicholas revealed an overall normal dipole structure, while the megaflash and TLE deep convective cases exhibited inverted dipole charge structures. Dissipation of the upper-level screening charge layer resulting from cloud top divergence likely played a role in the observed TLE VHF sources escaping to altitudes exceeding 30 km.

Keywords: atmospheric electricity (3304), lightning (3324), tropical cyclones (3372), tropical convection (3371), instruments and techniques (3394)

Key Points

- A megaflash and several transient luminous events were observed as Hurricane Nicholas approached the Texas Gulf Coast.
- Strong cloud top divergence of air parcels, wind shear, and moisture impact the location and magnitude of lightning activity.
- Charge structure evolution in tropical deep convection reflects physical processes related to the likelihood of rare lightning events.

Plain Language Summary

Hurricane Nicholas impacted the Texas Gulf Coast over a two-day period on 13-14 September 2021. Nicholas moved inland southwest of Houston and rapidly weakened throughout the day on 14 September 2021. Counterclockwise winds moving around the eye along with upper-level winds flowing from the northwest enhanced the removal of air parcels at the top of the thunderclouds. This in turn helped to intensify updrafts necessary for thunderstorm development in the rainband and eyewall regions. The Houston Lightning Mapping Array, a network of lightning detectors, identified rare lightning activity in the rainband and eyewall regions of Hurricane Nicholas. The thunderstorms in the rainband produced a large, curved "megaflash" lightning bolt that was 220 km across at 2004 UTC on 13 September 2021. Nicholas was designated as a Category 1 hurricane at 0000 UTC on 14 September 2021. Vigorous eyewall lightning activity developed more than two hours later which produced rarely observed lightning in the form of jets of electric charges called transient luminous events from 0230-0300 UTC on 14 September 2021. This type of lightning travels upwards from the tops of the thunderclouds towards space and helps to balance charges between the upper and lower atmosphere.

1. Introduction

The intensification or weakening tropical of cyclones (TCs) can be assessed by examining the evolution of electrified deep convection that develops within the TC (Boggs et al., 2018; Corbosiero & Molinari, 2002; Liu et al., 2015; Logan, 2021; Lu et al., 2011; Pan et al., 2020; Schultz et al., 2015; Solorzano et al., 2018; Tessendorf et al., 2007; Wiens et al., 2005; Xu et al., 2017). Though not all TCs generate an appreciable amount of lightning, the presence of electrified deep convection within a TC can indicate complex interactions between dynamic and microphysical processes (Pan et al., 2020). The environmental conditions that facilitate charging in a TC are intricate and extensively researched (Black & Hallett, 1986; Cecil & Zipser, 1999; Cecil et al., 2002; Corbosiero & Molinari, 2002; DeHart & Bell, 2020; Fierro et al., 2015; Fierro & Mansell, 2017; Frank & Ritchie, 2001; Han et al., 2021; Hu et al., 2020; Leighton et al., 2020; Logan, 2021; Pan et al., 2020; Wood & Ritchie, 2015). Some TCs exhibit more lightning than others due to competing effects of (a) thermodynamic variables such as convective available potential energy (CAPE) and available moisture, (b) cloud microphysics such as aerosols, supercooled liquid water, and ice particle concentrations, and (c) dynamic processes such as updraft strength, wind shear, and influence of synoptic boundaries (Cecil & Zipser, 1999; Corbosiero & Molinari, 2002; Hu et al., 2020; Liu et al., 2015; Logan, 2021; Molinari & Vollaro, 2009; Pan et al., 2020).

For example, Hurricane Harvey (2017) was one of the most electrified TCs on record (Logan, 2021; Pan et al., 2020). The Logan (2021) and Pan et al. (2020) studies investigated the influence of synoptic boundaries and aerosols on lightning activity during Harvey. A decaying stationary front provided additional moisture and lifting to initiate a broad area of electrified deep convection near the Texas Gulf Coast. In particular, it was shown by observation and

modeling that industrial-derived aerosols played an important role in increasing the population of ice and supercooled liquid water hydrometeors. This in turn led to a two-fold enhancement of lightning activity when compared to a "clean" scenario.

Hurricane Nicholas was designated as a Category 1 TC on the Saffir-Simpson Scale by the National Hurricane Center (NHC) at 0000 UTC on 14 September 2021 with a maximum sustained wind speed of 33 m s^{-1} and minimum pressure of 988 mb (Latto & Berg, 2022). Nicholas passed within range of the Houston Lightning Mapping Array (HLMA), which captured the overall lightning activity of convection within the eyewall and rainband along with two notable events: (i) what appeared to be a curved megaflash on 13 September 2021 and (ii) several high-altitude "jet-like" transient luminous events (TLEs) on 14 September 2021.

A megaflash is defined as a lightning flash with a spatial extent of 100 km or greater (Peterson, 2021; Peterson et al., 2022; Peterson, 2023). Megaflashes typically occur in the stratiform region during the transition of a deep convective event to a mesoscale convective system (MCS) and initiate in and around regions of low-level (< 7 km) positive charge or inverted charge structures (Lyons et al., 2020; Peterson, 2023). The dynamic and microphysical mechanisms of how megaflashes occur in MCSs are still under much scrutiny, especially considering recent discoveries of the longest lightning flashes in the world (Lyons et al., 2020; Peterson et al., 2021; Peterson et al., 2022). Nevertheless, observing one during a tropical cyclone event is nearly unprecedented, though Lyons et al. (2020) and Peterson (2023) pointed out that megaflashes may not be uncommon given the recent advent of sophisticated space-based lightning detection sensors (e.g., Geostationary Operational Environmental Satellite (GOES) geostationary lightning mapper (GLM)).

Jets (e.g., blue and gigantic jets) are TLEs that occur just above the cloud tops of vigorous thunderstorms and extend into the mesosphere (Boggs et al., 2022). They are typically observed during a period of decreasing lightning flash rates with a corresponding increase in charge layer height and may infer TC intensification (Boggs et al., 2018; Liu et al., 2015). High-altitude electrical activity (i.e., charge layer altitudes exceeding 15 km) typically indicates the presence of ice particles with broad size distributions in a dynamic environment of strong turbulent updrafts (exceeding 10 m s^{-1}), cloud top radial divergence in the vicinity of the updraft, and wind shear (Boggs et al., 2018; Boggs et al., 2022, Takahashi, 1978). The dynamic motions can enhance ice particle collisions (e.g., snow/graupel/hail) necessary for charging in the presence of supercooled liquid water (e.g., non-inductive charge mechanism) (Boggs et al., 2018; Wang et al., 2018; Wang et al., 2021).

This study employs measurements from the HLMA along with additional lightning, meteorological, satellite, and radar products to address the following scientific questions:

(1) What are the key dynamic and microphysical processes that led to the generation of the TC deep convective cells responsible for the rare lightning events?
(2) How can charge structure information of the TC deep convective clouds be used to elucidate the observed rare lightning events?

2. Data and Methodology

The preferred location of electrified deep convection within tropical cyclones is related to dynamic variables such as the magnitude and orientation of wind shear, storm relative helicity, and the overall propagation direction of the TC (Chen et al., 2006; Corbosiero & Molinari, 2002; Didlake & Kumjian, 2017; Frank & Ritchie, 2001; Homeyer et al., 2021; Latto & Berg, 2022;

Molinari & Vollaro, 2009; Stevenson et al., 2016). Moreover, TLEs imply the presence of an extensive upper-level negative charge layer which screens an underlying positive layer (Boggs et al., 2018; Boggs et al., 2022). Liu et al. (2015) suggested that erosion of the negative screening layer due to upper-level divergence (e.g., detrainment of air parcels near the cloud top) can aid in negative leaders escaping upward to the ionosphere, as observed during Hurricane Dorian. Hence, this study adopts the methodologies of Liu et al. (2015), Boggs et al. (2018), and Boggs et al. (2022), along with a charge analysis following the method of Medina et al. (2021) to evaluate the charge layer characteristics of the rainband and eyewall convection observed during Nicholas.

2.1 Houston Lightning Mapping Array (HLMA)

The Houston Lightning Mapping Array (HLMA) consists of a network of very high frequency (VHF) time-of-arrival (TOA) lightning mapping sensors. The sensor network encompasses the entirety of the Houston metropolitan area and detects nearly 100% of total lightning occurring within a 100 km radius from the centroid (29.76°N, 95.37°W) (Cullen, 2013; Logan, 2021). The HLMA network has undergone upgrades (e.g., the addition of sensors and hardware improvements) since 2020 which has helped to extend the detection of VHF source points to nearly 400 km from the HLMA centroid with a detection efficiency exceeding 70% up to 250 km (see Figure 1 in Logan, 2021). This also includes increased coverage over the remote Gulf of Mexico. The uncertainty of VHF source detection rapidly increases with the square of the range away from the centroid (Thomas et al., 2004; Weiss et al., 2018). There are two factors to consider regarding source points located much greater than 100 km away from the centroid: (a) the number of detectable VHF sources located high up in the deep convective cloud and (b) the minimum number of sensors needed to detect VHF sources to be processed as a legitimate

data point. Thus, the detection efficiency of VHF sources is highly contingent upon the robustness of the deep convection and uniformity of VHF source point emissions (Weiss et al., 2018).

Lightning mapping software such as XLMA (e.g., a proprietary software developed by New Mexico Tech for reading lightning mapping data files) is used to manually analyze the charge structure of VHF source data retrieved by the sensors (Thomas et al., 2004). The leader initiating the flash propagates through regions of positive and negative charge. Positive charge regions (negative leaders) are "noisier" than negative charge regions (positive leaders) and are subjectively identified using XLMA along with lightning flash polarity and peak current data retrieved from the National Lightning Detection Network (NLDN) (Cummins et al., 1998; Murphy et al., 2021). Thunderstorms can have anywhere from a few dozen to thousands of flashes per hour, which proves to be a tedious task to analyze manually. The number of VHF source points constituting flash size is sorted by XLMA to discern big (>75 sources), medium (>10 sources), and small flashes (<10 sources). Hence, for a deep convective event with thousands to millions of source points, it is expedient to analyze the charge structure using big flashes. However, it is possible to lose a great deal of information about the storm evolution since big flashes are only observed during certain periods in a convective event.

The raw VHF source data are quality-controlled by using XLMA to remove questionable and mislocated source points using the chi-square parameter (χ^2) which minimizes errors in geolocating the sources (Thomas et al., 2004). However, TLEs and other anomalous lightning events may likely be hidden in what is considered erroneous VHF source data. Therefore, this study incorporates the following data constraints: (a) the χ^2 value is set to 2 to ensure location and timing accuracy and (b) the minimum number of HLMA sensors is set to 7 to ensure enough

159 sensors observed the same VHF source events for higher data quality (Lyons et al., 2020). The
160 VHF source data are then sorted into flash groups using algorithms developed by Bruning &
161 MacGorman, (2013) and Fuchs et al. (2015) (e.g., "lmatools" Python-based software package).
162 These algorithms constitute VHF lightning sources within 3 km (i.e., considering a three-
163 dimensional plane) and 0.15 s of one another into a flash and can differentiate between other
164 sources and flashes. This study uses both VHF source (primary TC analysis) and flash level data
165 (secondary charge layer analysis) as proxies for dynamical and microphysical properties which
166 are detailed further in the following sections. All VHF sources are filtered through the chi-
167 square/sensor method used in this study since upper atmosphere VHF source points (>15 km) are
168 sometimes identified as mislocated pulses above the cloud top. To observe the full TLE, the
169 altitude must be changed from a default limit of 20 km to a limit of the highest detectable source
170 point believed to be part of the TLE (e.g., 45 km in this study). Therefore, observed VHF source
171 points above 20 km that are not eliminated by quality control filtering are included. In addition,
172 the lmatools package is tunable in that the number of sensors, χ^2 values, and distance from the
173 LMA centroid can be adjusted to account for TLEs. Note that the distance used in this study is
174 300 km.

175 2.2 Charge Analysis

176 A typical thunderstorm will have at least two oppositely charged layers depending on the
177 direction of propagation of the negative or positive leader after initiation (Chmielewski et al.,
178 2018; Medina et al., 2021; Williams, 1985). A normal dipole charge structure consists of an
179 upper-level positive charge layer overlying a negative charge layer, while an inverted dipole
180 structure is the opposite (Stolzenburg & Marshall, 2009). A normal tripole structure consists of a
181 negative charge layer sandwiched between two positive charge layers, with an inverted tripole

structure being the opposite (Stolzenburg & Marshall, 2009). Therefore, dipole and tripole charge structures indicate possible abnormalities during a thunderstorm's life cycle (Medina et al., 2021; Tessendorf et al., 2007).

ChargePol is an objective, automated method that ingests the data output from the lmatools package (e.g., LMA flash level data) to determine lightning flash polarity, charge layer altitude, and vertical distribution of charge layers during the life cycle of electrified deep convection (Medina et al., 2021). ChargePol not only reduces the analysis time of lightning flashes, but it can also estimate the altitude and thickness of positive and negative charge layers. Note that the analysis comes at the expense of only being able to analyze a fraction of the lightning flashes compared to the number of detectable lightning flashes by the NLDN. As discussed by Medina et al. (2021), the algorithm is sufficient to provide a general picture of the flash count, polarity, and charge structure of the deep convection being analyzed. The charge structure evolves over time and in some cases, starts as "normal" and then becomes inverted or vice versa (e.g., RELAMPAGO case studies presented in Medina et al., 2021). The height of the positive and negative charge layers also temporally evolves and is used to illustrate the storm's life cycle.

ChargePol has the versatility of tunable parameters such as adjusting the number of sources which constitutes a flash upward or downward with respect to a default value of 10. In addition, the default percentile interval to define a charge layer includes a 10^{th}-90^{th} range. This study lowers the minimum number of sources to 5 while increasing the percentile range to include the 5^{th} and 95^{th} percentiles to account for the furthest distance of the center of Nicholas from the HLMA centroid (~400 km), as well include as many usable VHF source data points from the convective cells as possible. A subjective "lasso" method is employed by using XLMA

to construct a polygon around the densest region of collocated VHF source points as well as added datasets from ChargePol flash output and NLDN lightning flash information from the rainband and eyewall of Nicholas. This offers a fortuitous opportunity to dissect the spatiotemporal electrical nature of individual cells, individual cells within a group of storms, or an entire deep convective event using data from multiple independent lightning datasets.

2.3 NEXRAD products

Deep convective cloud hydrometeor structure and distribution are well illustrated by radar reflectivity products (Fridlind et al., 2019; Handler & Homeyer, 2018; Hu et al., 2020; Steiger et al., 2007). Lightning activity is generally inferred by the presence of the 30 dBZ echo layer typically at a height several kilometers above the melting level (Carey & Rutledge, 2000; Logan, 2021; Petersen & Rutledge, 2001; Stolz et al., 2014; Wang et al., 2018). At this altitude, it is assumed that there is an abundance of supercooled liquid water and mixed populations of large and small ice particles (e.g., graupel, hail, snow, rimed ice, etc.). The ice particles will collide and exchange charges as long as the environmental temperature is between -10°C and -40°C (Mecikalski et al., 2015). Given updraft speeds exceeding 5 m s^{-1}, sufficient turbulence in tropical convection (e.g., Cecil & Zipser, 1999) will carry smaller positively charged ice particles to upper regions of the deep convective cloud, while larger ice particles will fall to the base of the cloud facilitating a negative charge ultimately leading to a lightning discharge (e.g., cloud-to-ground or intracloud).

Next Generation Radar (NEXRAD) products are used in this study to illustrate the spatiotemporal evolution and movement of hydrometeors in electrified deep convection (Crum & Alberty, 1993). The products include base reflectivity (Z_h) and dual polarization products such as differential reflectivity (Z_{dr}), differential phase (k_{dp}), correlation coefficient (ρ_{hv}), cloud echo top

height, radial divergence, and hydrometeor classification (Handler & Homeyer, 2018). A gridded NEXRAD product (GridRad) is utilized to analyze the cross-section altitude of the radar volume scans (Homeyer & Bowman, 2023) in relation to the HLMA observations of charge layers. GridRad-derived radial divergence follows the method of Sandmael et al. (2019) which merges the azimuthal and radial components of NEXRAD retrieved wind velocity. Errors include general retrieval uncertainty (e.g., 0.004 s^{-1}) and aliasing due to the radial derivative of wind velocity (V_r) exceeding the maximum detectable value (e.g., Nyquist velocity). The Sandmael et al. (2019) method is used to de-alias the V_r component and thus lower uncertainty in the GridRad radial divergence product (Homeyer & Bowman, 2023). GridRad features a 5-min temporal resolution along with a spatial resolution of (0.02º x 0.02º x 1 km). The lightning datasets discussed in Section 2.1 can be overlain onto the plan and cross-section GridRad plots to better illustrate the 4-dimensional (e.g., longitude, latitude, altitude, and time) electrical and microphysical nature of deep convection (Logan, 2021). The HLMA lightning source and flash level data are scaled to match the spatial and temporal resolution of GridRad output in this study.

2.4 Meteorological Analysis

To quantify the dynamic/thermodynamic conditions during the evolution of Nicholas, atmospheric sounding data used in this study include environmental and dewpoint temperature profiles, surface and most unstable (MU) convective available potential energy (CAPE), wind speed and direction profiles, low-level (1-3 km) and mid-level (3-6 km) wind shear, and storm-relative helicity (SRH). Since Nicholas intensified and made landfall primarily between Corpus Christi (CRP) and Lake Charles (LCH), National Weather Service (NWS) soundings at those locations along with rapid refresh (RAP) model soundings are used to further examine the environmental conditions (e.g., melting layer height and humidity profile) relative to areas of

rainband and eyewall convection. Special attention is paid to the environmental conditions during the megaflash and TLE cases. The NHC Tropical Cyclone Report (Latto & Berg, 2022) is used as ground truth for summarizing the TC stages from tropical storm to hurricane status, while the NOAA hurricane database (HURDAT2) product (Landsea & Franklin, 2013) is used to quantify the location of the eye/eyewall, wind speed, and central pressure for Nicholas.

3. Results

3.1 Summary of initial development and electrical nature of Nicholas

According to Latto & Berg (2022), Nicholas was disorganized when it initially developed. The TC was steered northward by a subtropical ridge located in the eastern Gulf of Mexico. Figure 1 shows the VHF source rate, charge region heights, spatiotemporal VHF source density, and ChargePol charge analysis during the entire life cycle of Nicholas from 12-14 September 2021. A total of 443,126 VHF sources were identified by the HLMA. There was ongoing convection along the Gulf Coast prior to 1200 UTC on 12 September 2021 (Figure 1a, black line). At 1200 UTC, Nicholas was officially designated as a tropical storm with a central pressure of 1008 mb. Electrified deep convection began to intensify after 1800 UTC with a VHF source rate increasing to just over 6000 sources $(5\ \text{min})^{-1}$ (see Figure 1a). By 0000 UTC on 13 September 2021, the center Nicholas had reformed twice and moved northeastward as the ridge began to weaken. There was never an observable eye with Nicholas from GOES satellite imagery, although GridRad reflectivity data revealed discernible eyewall convection and structure by 1700 UTC as Nicholas moved closer to the Texas Gulf Coast within the range of the Houston (KHGX) and Corpus Christi (KCRP) radar platforms (Supplemental Movie 1).

As shown in Figure 1, after 1700 UTC on 13 September, rainband lightning activity intensified and lasted until Tropical Storm Nicholas (blue TS) was upgraded to a Category 1 hurricane (red H and green line) with a central pressure of 998 mb and the center of circulation approaching 28^{o}N (Figures 1c and 1d). Rainband lightning activity began to diminish as lightning activity within the eyewall became more prominent 0000 UTC on 14 September 2021. At this time, the central pressure of Nicholas had decreased to the lowest observed value of 988 mb. At 0100 UTC, the VHF source rate increased to the highest value of the entire event (~10,600 sources (5 min)$^{-1}$) (Figures 1a and 1c). In addition, the charge layer altitude noticeably increased. There was a decline in lightning activity after 0230 UTC and a final round of weak electrified convection developed as Nicholas officially made landfall at 0530 UTC (gold line) while the central pressure rose to 991 mb at that time. Figure 1b presents a depiction of the height distribution of VHF sources normalized to the maximum value of sources (gray line). The overall most probable height of the VHF sources during Nicholas was roughly 8 km, which corresponded to a temperature of -18^{o}C according to the LCH and CRP soundings from 1200 UTC 12 September to 1200 UTC 14 September. A small contribution of upper-level VHF sources was apparent by the upper "tail" of the altitude distribution above 15 km. A detailed discussion of the ChargePol charge analysis (positive and negative regions) is presented in section 4.2. Figure 1d shows a lightning footprint of Nicholas which includes a broad area of lightning activity in the primary rainband region along with pockets of electrified convection closer to the Gulf Coast and includes smaller lightning hotspots near the main track of the center of circulation (e.g., eyewall). The presence of VHF source points well above the 10 km altitude in the smaller longitudinal and latitudinal boxes lies near a location of 28.5^{o}N and 96^{o}W which is close to the eyewall track.

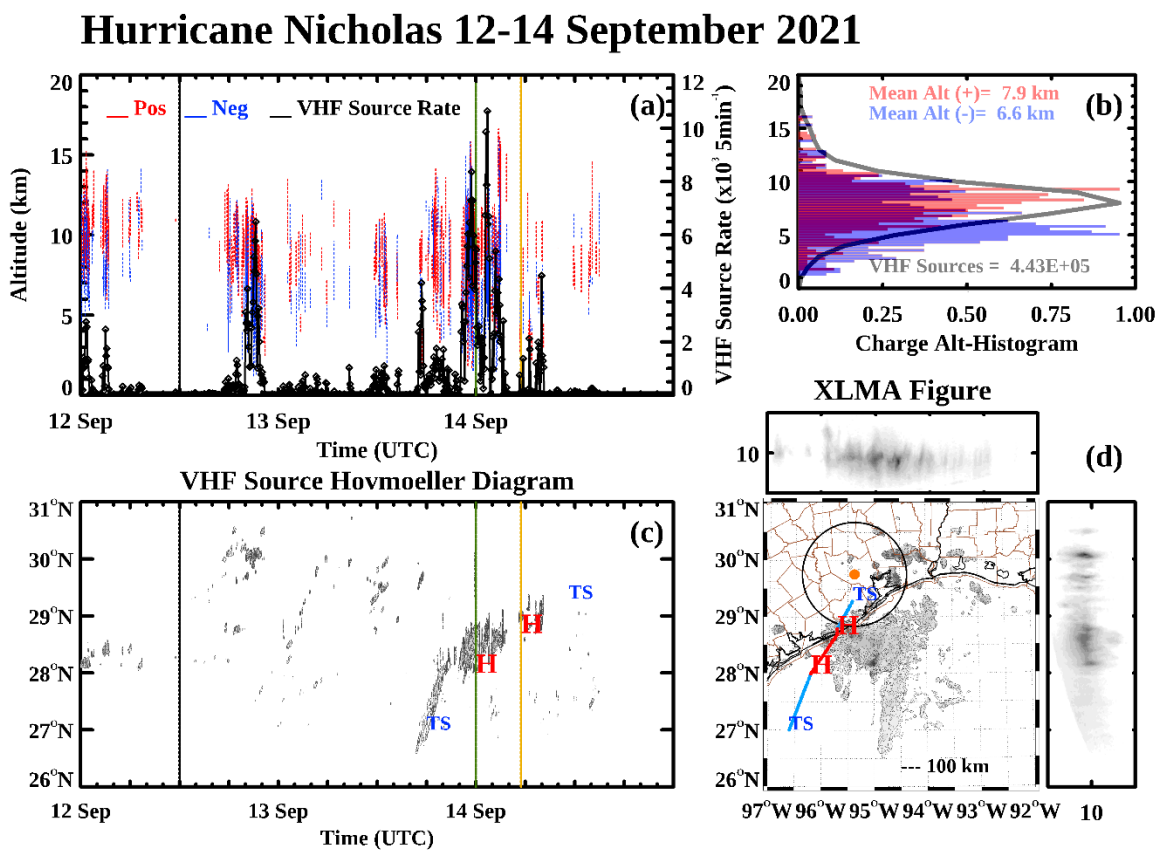

296

297 **Figure 1.** (a) ChargePol flash polarity and altitude (primary y-axis) and VHF source rate (in
298 thousands) on the secondary y-axis. Tropical storm status (black line), hurricane status (green
299 line), and landfall (gold line) are indicated. Major tick marks (secondary x-axis) are every six
300 hours. (b) Height distribution of all VHF sources (gray line) along with ChargePol positive (red)
301 and negative (blue) charge regions. (c) Hovmoeller diagram of VHF source density. The times of
302 tropical storm (blue "TS") and hurricane (red "H") status are shown at the respective latitude of
303 the center of circulation (NOAA HURDAT2). (d) "XLMA" style figure showing overall VHF
304 source density (plan view), longitude-altitude (top box) and latitude-altitude (right box). The
305 black circle indicates a 100 km radius from the HLMA centroid (orange circle). The NOAA
306 HURDAT2 TC track is overlain.

307 3.2 Rainband and Eyewall

308 The lasso method was used to select the highest concentration of VHF sources resulting
309 from electrified deep convection within the rainband and eyewall as shown in Figures 2 and 3,
310 respectively. The VHF source rate initially peaked at roughly 1200 sources $(5\ min)^{-1}$ from 1700-
311 2000 UTC on 13 September resulting from weak rainband convective activity that propagated

northward over time (Figures 2a and 2c). As the VHF source rate declined, a megaflash occurred in the outer rainband region at 2004 UTC (Figures 2c and 2d). The VHF source rate then increased substantially to around 5,100 sources $(5\ min)^{-1}$ during the period from 2200-2300 UTC on 13 September 2021 as the strongest convective cells within the rainband developed. Charge layer altitude increased during this time. There was a secondary peak in VHF source rate (~3,300 sources $(5\ min)^{-1}$) at 0200 UTC on 14 September 2021 resulting from the additional development of deep convective cells located in the northeast region of the rainband (Figures 2c and 2d).

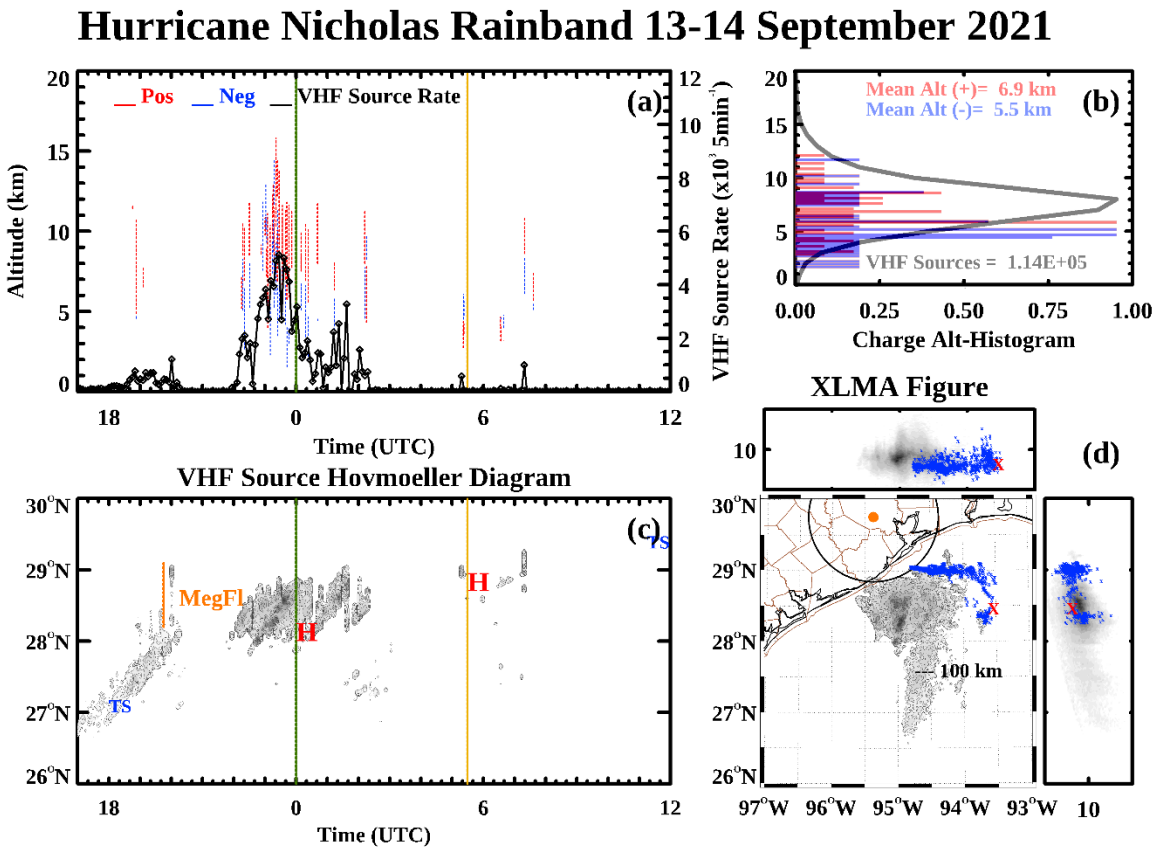

Figure 2. Same as Figure 1 but only includes rainband VHF sources from 1700 UTC 13 September 2021 to 1200 UTC 14 September 2021. Major tick marks (secondary x-axis) are hourly. The megaflash (MegFL) is included in (c) and the blue VHF source points of the megaflash are overlain in (d). The initial megaflash VHF source point at 2004 UTC on 13 September 2021 is denoted by the red "X".

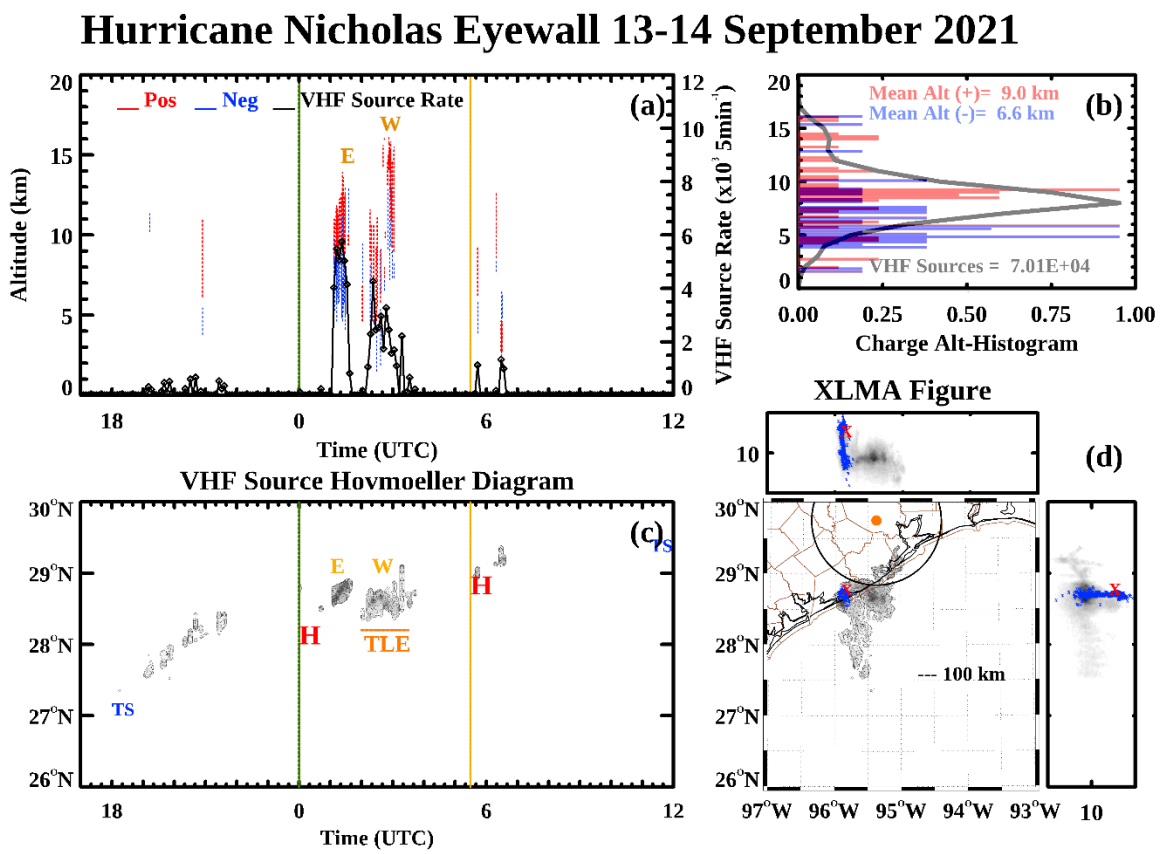

Figure 3. Same as Figure 2 but only includes the eyewall VHF sources. The time span (orange line) of the TLE cases is included in (c) and the blue VHF source points of the TLE Case I are overlain in (d). The initial Case I VHF source point at 0239 UTC on 14 September 2021 is denoted by the red "X". "E" and "W" highlight eastern and western eyewall electrified cellular convection.

There were two distinct bursts of eyewall lightning corresponding to the eastern and western regions (Figure 3a). Figure 3c showed that as Nicholas propagated northeastward, there was little to no electrical activity before 0100 UTC on 14 September. The VHF source rate increased rapidly to a peak of 5,600 sources $(5\ min)^{-1}$ in the eastern eyewall region at 0130 UTC. At 0200 UTC, the convection migrated northward and westward around the eyewall and re-intensified in the western eyewall region yielding a VHF source rate of ~4,500 sources $(5\ min)^{-1}$ by 0230 UTC. Several TLEs were observed by the HLMA between 0230-0300 UTC as the VHF source rate declined. The final round of weak lightning activity occurred after 0530 UTC with

VHF source rates diminishing to less than 1,500 sources $(5\ min)^{-1}$, indicating fewer electrified convective cells and rapid weakening of the tropical cyclone (e.g., rise in minimum central pressure).

Though the most probable heights of the eyewall and rainband lightning were similar (~8 km), there was a higher frequency of sources above 15 km in the western eyewall region than both the eastern eyewall and rainband regions (Figures 2b and 3b). Additionally, two features were apparent: (i) the increase in the rate of VHF sources in the rainband preceded the upgrade of Nicholas to hurricane status and (ii) the highest VHF source rates occurred in the eyewall region after Nicholas became a hurricane. The differences between the rainband and eyewall electrification with respect to the overall charge structure of Nicholas are discussed further in Section 4.2.

3.3 Megaflash and TLEs

Figures 4-8 show the spatiotemporal nature of electrical activity of the megaflash and four TLE cases along with corresponding GridRad plan and cross-section reflectivity scans encompassing the approximate case times. In addition, all five lightning flash cases have been animated and their respective charge layers were manually analyzed using XLMA. The animations are provided in Supplemental Figures 1-5. A brief description of the charge analysis is presented in the following subsections.

3.3.1 Megaflash Case

Figure 4 shows a curved megaflash which occurred at approximately 20:04:56 UTC on 13 September 2021. The first VHF source point was located at 6 km, lasted for nearly 1.6 s (Figure 4a), and was initially associated with a negative intracloud stroke. Two more negative

intracloud strokes followed and the last recorded intracloud stroke was positive. Of the five ground flashes, the first two were denoted by the two positive peak current strokes of 94 and 161 kA. The next two ground strokes were also positive while the final stroke was negative. As shown in Figures 4b and 4c, most of the positive VHF source points were located between the melting level and the -10^{o}C isotherm (6 km) while negative VHF source points were concentrated at ~8-9 km in a colder region (<-20^{o}C). The negative intracloud and strong positive ground strokes at the time of the megaflash lend support to manual analysis which revealed the presence of an inverted dipole with some evidence of an inverted tripole.

Figures 4b and 4e illustrate that the vast majority of VHF source points comprising the megaflash were located in the stratiform region of the outer rainband convection. That is, the radar reflectivities at the altitudes of the VHF source points were less than 35 dBZ, and no source points were observed above the glaciated level (-40^{o}C). Figure 4d shows that the VHF source points exhibited a bidirectional propagation away from the initial point. When animated by XLMA (Supplemental Figure 1), a small pocket of sources (black/blue symbols) first appeared south of the white "X" (28.5^{o}N, 93.4^{o}W) with the northern and western source points (e.g., blue, purple, green, orange, and red symbols) appearing after. Furthermore, the megaflash traveled a straightened distance of nearly 220 km.

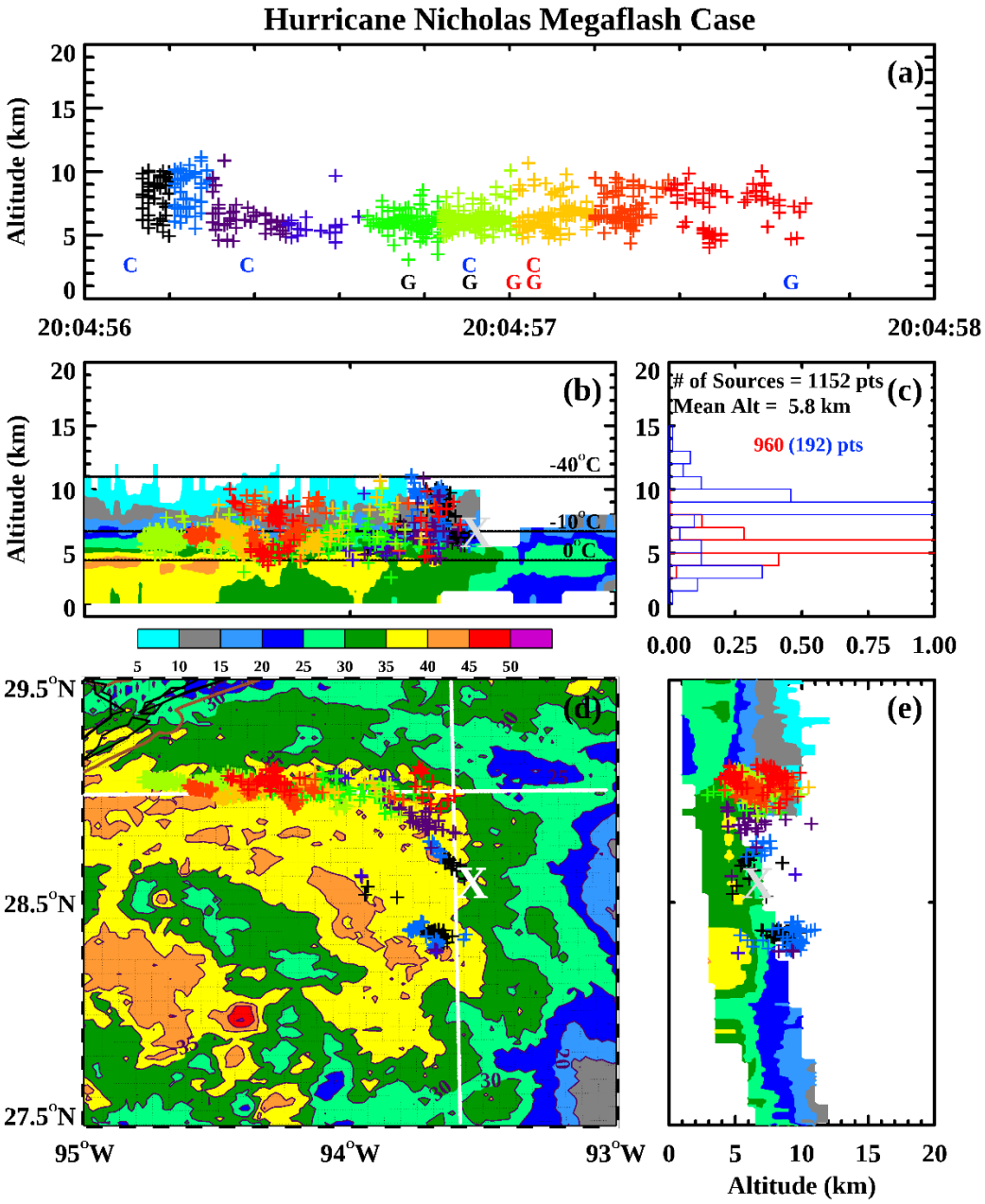

380

381 **Figure 4.** "XLMA" style figure showing (a) Progression of VHF sources color-coded by time,
382 NLDN intracloud (C) and ground (G) strokes color-coded by polarity, (b) Longitude-altitude plot
383 of VHF sources and GridRad reflectivity overlaid with the environmental temperatures from the
384 LCH site, (c) VHF source distribution, mean altitude, and manually-analyzed polarity of the
385 charge layers, along with the cumulative density of positive (red line) and negative (blue line)
386 sources, (d) GridRad plan view with overlain VHF sources. Cross-section latitude and longitude
387 are denoted by white lines with the initial point of flash denoted by the white "X", (e) Latitude-

388 altitude plot of (b). The black NLDN ground strokes denote positive peak current values
389 exceeding 90 kA.

390

391 3.3.2 TLE Cases

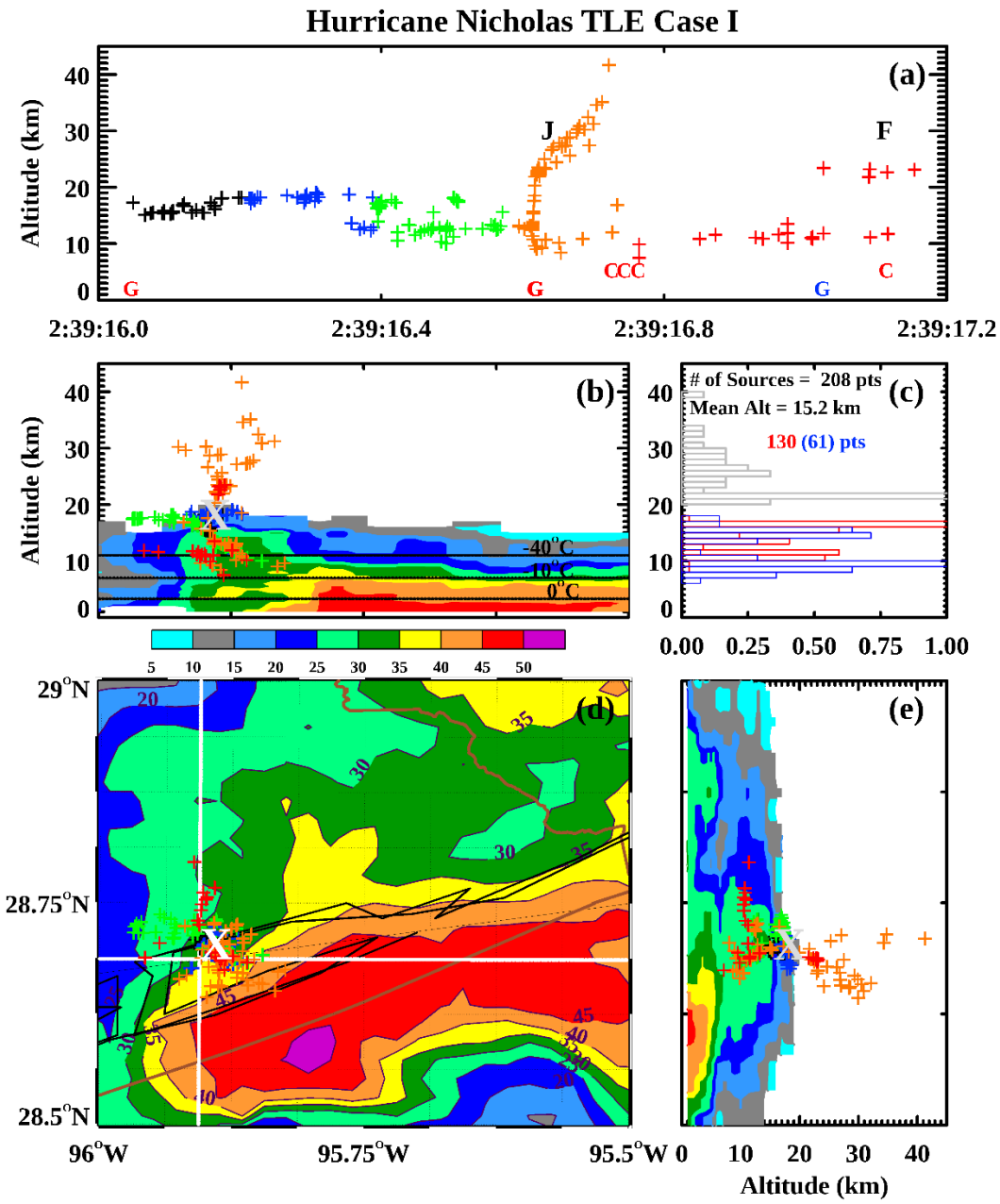

392

393 **Figure 5.** Same as Figure 4 but for TLE Case I. "J" denotes a possible jet TLE while "F" denotes
394 a failed "bolt from the blue" (BFB). Note that charge altitude in (c) is adjusted to include VHF
395 sources beyond 20 km (gray).

396 Case I featured a lightning flash exhibiting a "jet-like" plume of VHF source points ("J")

397 at approximately 02:39:16 UTC on 14 September 2021 (Figure 5a). The initial VHF source point

398 appeared at 14 km and the flash lasted for nearly 1.2 s. The actual jet occurred at approximately

02:39:16.6 UTC and reached a maximum altitude of 40 km. A few failed "bolt-from-the-blue (BFB)" discharges ("F") (e.g., Lu et al., 2011) followed the jet at approximately 02:39:17.0 UTC. Failed BFBs can precede or follow a jet. They are denoted by VHF source points having an inverted "L" shape configuration and are thought to discharge completely within the cloud and not reach the ground. When animated, the jet reached a maximum altitude of 40 km nearly 700 ms into the flash (Supplemental Figure 2). There were four ground strokes with the first one of positive polarity occurring at the time of the initial VHF source. Two positive ground strokes followed and were observed at the same time as the jet. Both strokes occurred within microseconds of one another and appeared as one stroke at 02:39:16.7 UTC. The final ground flash was observed during the period of failed BFBs and was negative. Four positive intracloud strokes were observed after the jet with the final intracloud stroke occurring during the period of the failed BFBs.

In Figures 5b and 5c, most of the positive VHF source points were located well above the glaciated level (-40^{o}C isotherm at 11 km) at ~17 km. The negative VHF source points peaked between 9-10 km (-30^{o}C). However, there was one notable negative charge layer at 15 km and a small screening layer at 19 km. The 0240 UTC GridRad scan indicated that the 30 dBZ reflectivity echo height exceeded 15 km in the vicinity of the initial flash source point (Figures 5b and 5e). Figure 5d shows that the TLE occurred within the northwest periphery of an intense deep convective core in the western eyewall region (>50 dBZ). It was evident that the cell featured an overall inverted dipole with hints of additional complex charge structures. Moreover, the skewed nature of the 35 dBZ reflectivity shown in the cross-sections (Figures 5b and 5e) suggested the presence of a highly sheared environment where the jet formed. The plume of VHF sources was depicted as an eastward leaning cone in Figure 5b and was oriented to the

south in Figure 5e. This was likely related to the counterclockwise motion of deep convective cells around the eyewall (Figure 5d).

Case II occurred nearly a minute later (02:40:48 UTC) and lasted for roughly 2 s. The initial VHF source point of the flash was located at 12 km and featured two jets (Figure 6a). The first jet occurred nearly 500 ms after the initial VHF source and reached a maximum altitude of 36.5 km. The second jet occurred at 02:40:49.4 UTC, or 1.4 seconds into the event and reached a maximum altitude of 24 km. A third jet may have also occurred at 02:40:49.7 UTC but the lack of source points at that time makes this claim uncertain. Failed BFBs were observed nearly 300 ms after the first jet and 500 ms before the second jet. There were four ground strokes with the first one of positive polarity occurring at the time of the first jet. A positive and negative ground stroke were both observed during the period of the BFBs while the final ground flash was observed during the second jet. Four intracloud strokes were observed with the first one occurring at the beginning of the flash. Two more occurred during the BFB period and the final occurred at the same time as the final ground stroke. Similar to Case I, all intracloud strokes were positive. Note that Case I and Case II share the same radar volume scan.

In Figures 6b and 6c, most of the positive VHF source points were above 11 km. The negative VHF source points peaked at 10 km. There was a notable positive screening layer at 19 km in contrast to Case I. However, Case II also featured an overall inverted tripole structure due to a small positive charge region (7 km) underlying the robust negative charge region (10 km). Figure 6d shows a more concentrated plume of VHF sources northwest of the convective core. In contrast to Case I, the plume of VHF source points exhibited a less noticeable orientation to the south and east (i.e., the source points were oriented straight upwards). The animation of Case II

(Supplemental Figure 3) illustrated the first jet providing a channel in which the second jet followed with some evidence of VHF sources from the third jet.

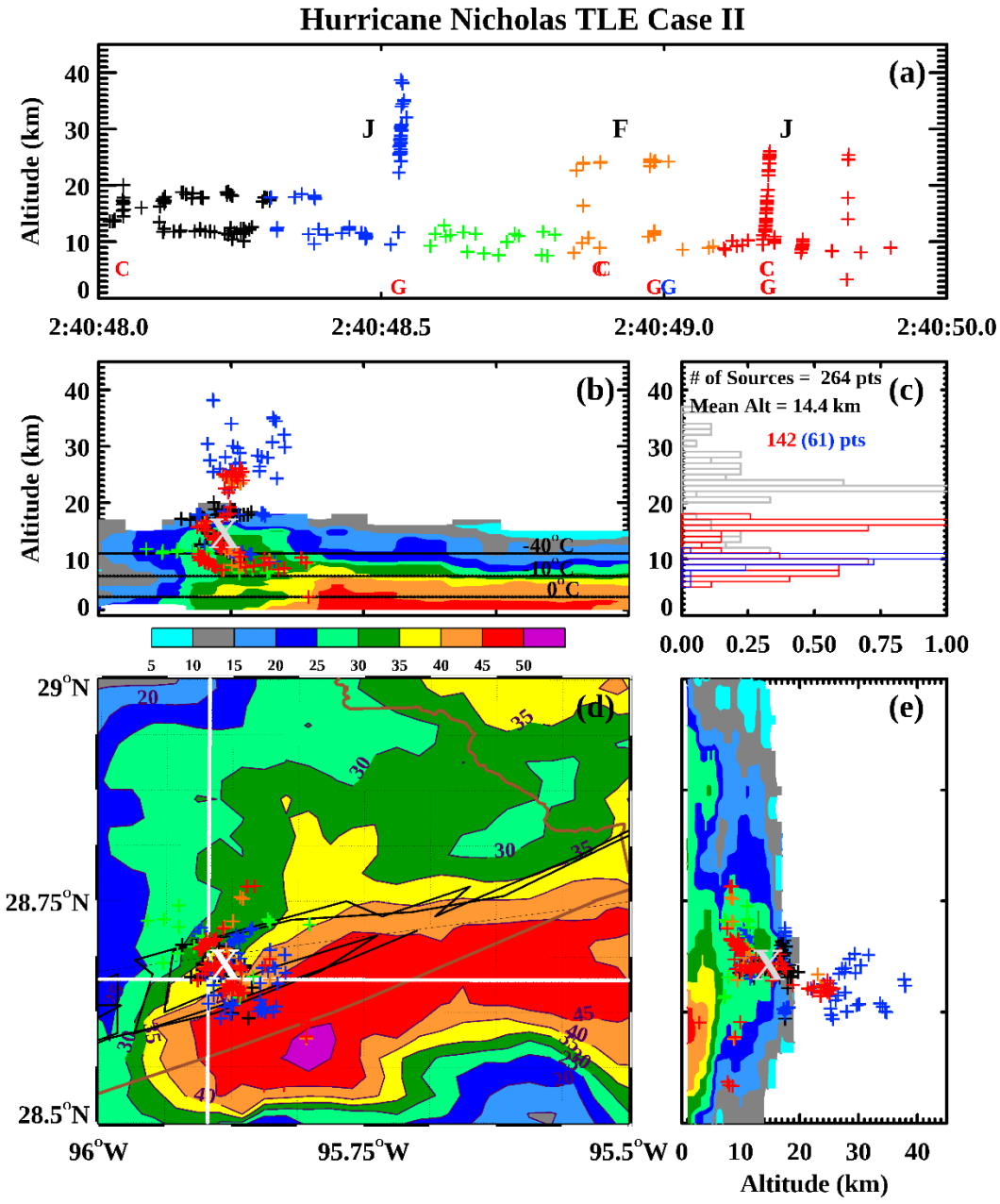

Figure 6. Same as Figure 5 but for TLE Case II.

449 The Case III flash lasted for nearly 2.5 s (Figure 7a). Case III featured two jets at
450 02:50:52.6 and 02:50:53.4 UTC along with a possible third jet just after 02:50:53.5 UTC. It is
451 not entirely evident that the first jet was continuous because (a) it terminated at an altitude of 21
452 km and (b) VHF sources approaching 42 km were observed nearly 200 ms after the initial
453 appearance of the jet. The second jet featured VHF sources reaching an altitude of 26 km. The
454 initial VHF source altitude was 12.9 km with no corresponding lightning strokes. There were no
455 discernible failed BFBs during the flash. Three ground strokes featured positive polarity with the
456 third one occurring at the time of the first jet. There were six intracloud strokes with the third one
457 occurring with the uppermost VHF sources. No strokes were associated with the subsequent jets.
458 This is not to say that there was no observable lightning, but that the NLDN was not able to
459 capture any ground or intracloud strokes at that time.
460 Figures 7b and 7c reveal VHF source points that were primarily clustered at or below the
461 glaciated level. There was an extensive upper charge region peaking at 15 km populated by a
462 mixture of negative and positive VHF sources with an underlying robust positive charge region
463 at 8 km. This case exhibited an inverted dipole charge structure and there was a slight negative
464 screening layer at 19 km. Figure 7d shows widely scattered VHF sources now collocated
465 southwest of the convective core (e.g., purple region of reflectivities). The apparent southward
466 and westward tilt of the cone-like projection of VHF sources, downshear of the convective core,
467 was also evident in Figures 7b and 7e (see Supplemental Figure 4). The cone-like projection of
468 the plume of VHF sources is nearly vertical in Figure 7e.
469

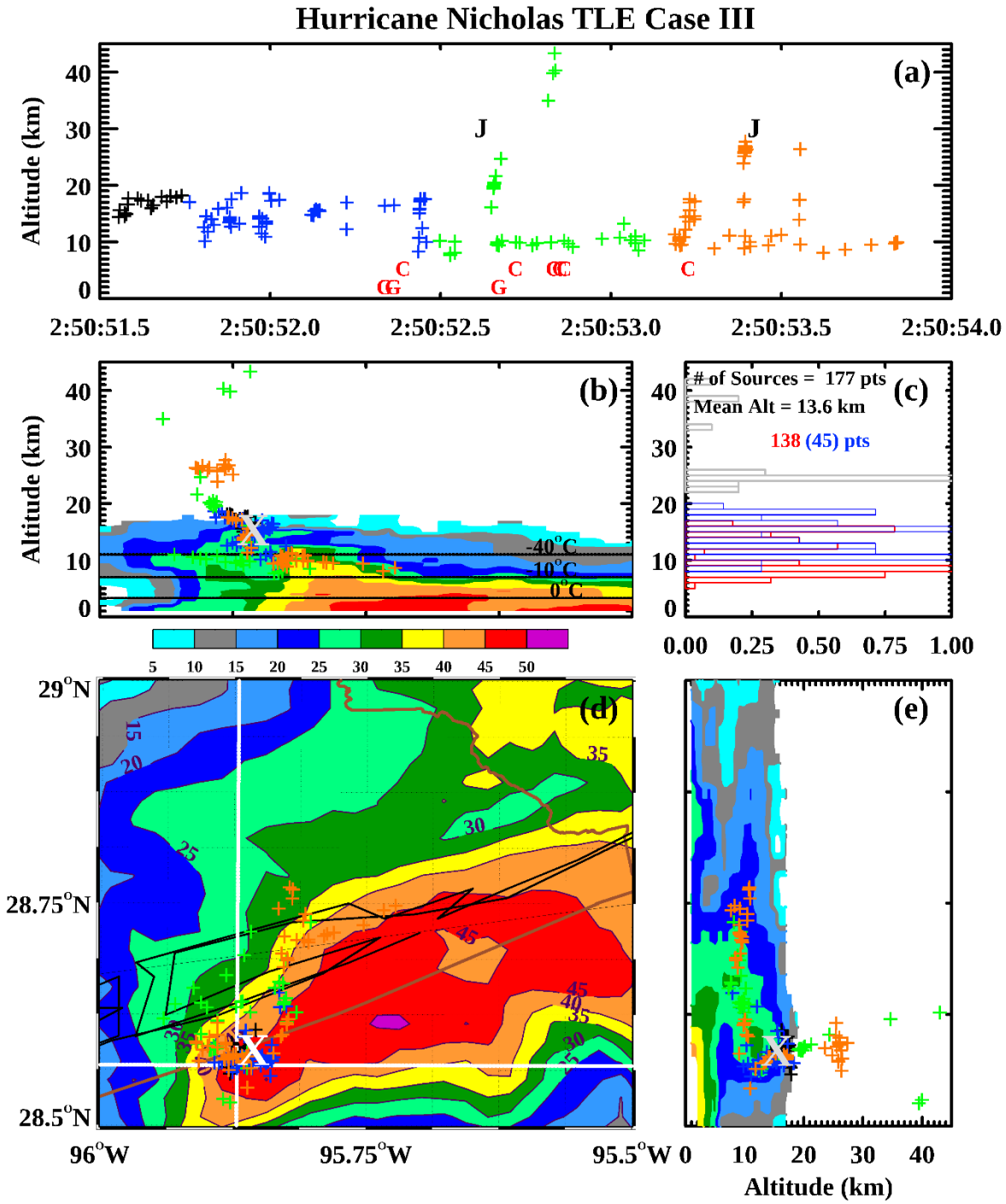

470

471 **Figure 7.** Same as Figure 5 but for TLE Case III

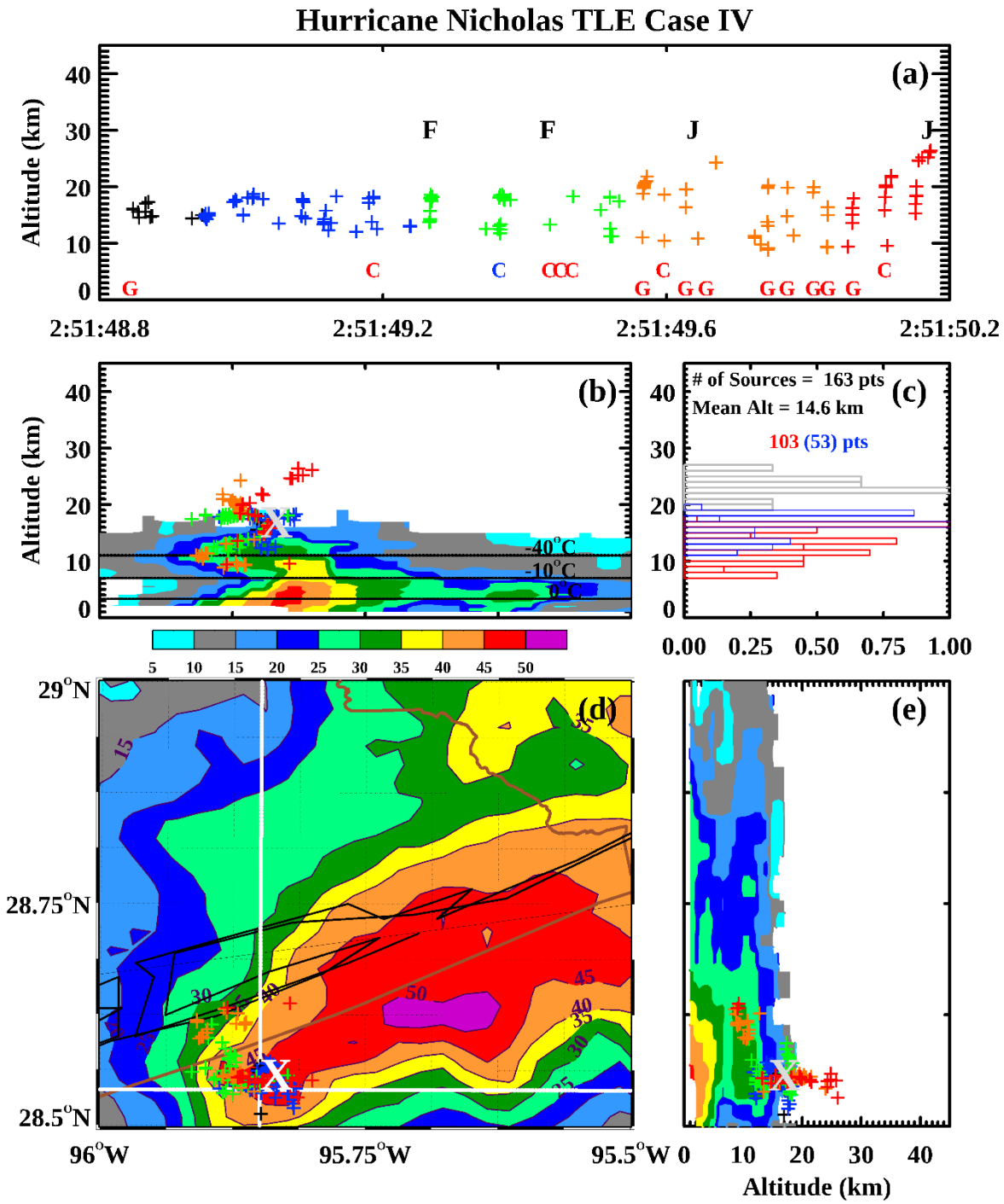

472

473 **Figure 8.** Same as Figure 5 but for TLE Case IV

474 The Case IV flash initiated at 14.2 km and lasted for 1.4 s. The flash featured a scarcely

475 discernible first jet just after 02:51:49.6 UTC and a second jet at 02:51:50.15 UTC following two

observed failed BFBs at 02:51:49.25 UTC and 02:51:49.35 UTC (Figure 8a). Note that the second jet occurred at the end of the flash. The VHF sources of the first and second jets reached 24.6 and 26.4 km in altitude respectively and represented the lowest maximum altitudes of all the TLE cases. The first and second jets also exhibited different orientations during their development (Supplemental Figure 5).

Figures 8b and 8c show VHF source points clustered above the glaciated level similar to Cases I and II. There was a notable upper negative charge region peaking at 17 km with an underlying deep positive charge region extending from 10-16 km. The upper screening layer from 19-20 km was robust and negative. This case was similar to the previous three cases by featuring an overall inverted dipole charge structure. The VHF sources were oriented westward of the convective core in Figure 8d, but the VHF sources in the jet were oriented east and south (Figures 8b and 8e). Figure 8e shows a cone-like configuration of VHF source points as in the previous cases. Moreover, the location of the initial point was the most southeastwardly displaced indicating the cyclonic motion of the eyewall deep convection (Figure 8d).

Case IV displayed prolific intracloud and ground strokes. There were seven intracloud and nine ground strokes which was the highest count of all the cases. The second intracloud stroke was negative and all other strokes were positive. The final two intracloud strokes occurred at the times of the two jets. One possible explanation is that the sheer amount of lightning could have acted to discharge the flash channel enough to reduce the maximum altitude of the jets. Moreover, the robust screening layer may have inhibited or “capped” the ability of VHF sources to achieve altitudes at or above the other three cases. The dynamic factors responsible for the electrical nature of the cases are detailed in the next section.

4. Discussion of rainband and eyewall lightning events

4.1 Meteorological conditions for the rainband and eyewall

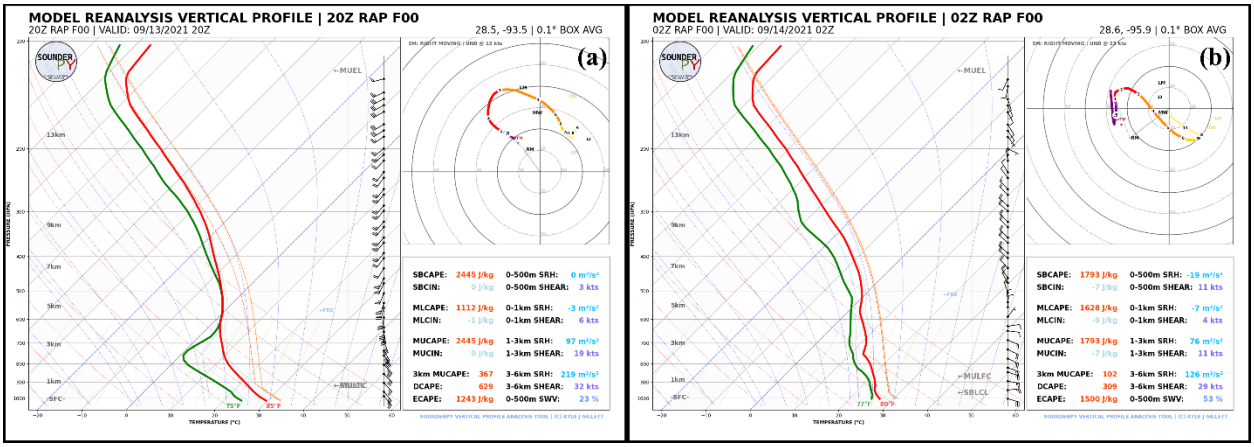

Figure 9. RAP forecast soundings representing the (a) 2000 UTC 13 September 2021 megaflash case and (b) 0200 UTC 14 September 2021 TLE cases. The soundings were generated via SounderPy (Gillett, 2024).

The RAP forecast sounding from 2000 UTC 13 September, taken from a grid point near the megaflash point of initiation (28.5°N, 93.5°W), was used to illustrate the dynamic and thermodynamic environment of the rainband during the megaflash case (Figure 9a). The surface convective available potential energy (CAPE) was 2445 J kg^{-1}. In addition, the mid-level (3-6 km) storm-relative helicity (SRH) was 219 m^2 s^{-2} and the low-level (1-3 km) SRH was 97 m^2 s^{-2}. The wind vectors veered from southeasterly to southerly with height from the surface up to around 9 km. The mid- and low-level wind shear values were 16.4 and 9.8 m s^{-1}, respectively. Furthermore, the relative humidity profile (not shown) near the surface (~70%) and above the melting layer (~90%) suggested moist conditions for much of the depth of the atmosphere. The CAPE values indicated updrafts capable of supporting robust electrified deep convection while the SRH values suggested embedded rotating cells.

Due to the veering low- and mid-level wind profiles, it is possible that a broad charge layer developed from turbulent deep convection near the eyewall and expanded northeastward

due to upper-level winds that were out of the southwest (Figure 9a). Over time, the charge layer was advected downward through gravitational settling as shown by the abundance of VHF sources near the melting layer (Figures 4b and 4e). In addition, the expansiveness of the charge layer may have been enhanced by secondary ice particles formed by collisions due to turbulence at or just above the melting layer (e.g., ice multiplication and splintering processes) (Black and Hallett 1986; Fierro and Mansell 2017; Hallett and Mossop 1974; Qu et al., 2022; Peterson, 2023). Furthermore, the cyclonic wind motion in the outer rainband may have acted to advect the cloud hydrometeor particles along with their intendant charge layer in a manner that warped the low-level charge region in which the megaflash initiated. That is, the discharge followed the orientation of the electric field resulting from the hydrometeor motions. Since there was only one megaflash observed, it is likely (a) the dissipation of electrical energy was sufficient to preclude further megaflash instances and (b) shortly after the megaflash occurrence, new convection developed within the rainband which not only reduced the stratiform region but also altered the charge structure needed for subsequent megaflash discharges. This is certainly grounds for future investigation.

For the eyewall TLE cases, the RAP sounding for 0200 UTC 14 September was taken from a grid point (28.6^{o}N, 95.7^{o}W) located near the eyewall (Figures 9b). The surface CAPE value was 1794 J kg^{-1}, the mid- and low-level SRH values were 126 and 76 m^{2} s^{-2}, respectively, and wind vectors backed northwesterly between 6-11 km. The mid- and low-level shear values were 14.9 and 5.7 m s^{-1}, respectively. The relative humidity profile (not shown) illustrated more moisture (> 80%) throughout the atmospheric depth. Similar to the megaflash environmental conditions, it is likely that strong mid- and upper-level updrafts were possible during the charging process before observance of the TLEs. Moreover, the upper-level northwesterly wind

vectors in the RAP soundings also help to explain the orientation of deep convection and location of the TLEs as well as the prominent southeastward displacement of the white "X" and plume of VHF sources shown in Figures 5-8. According to Corbosiero & Molinari (2002) and Molinari & Vollaro (2010), TC electrified deep convection is more favored in the eastern eyewall (e.g., downshear region of Nicholas). Mid-level shear values exceeding 10 m s^{-1} were present in the RAP profiles in the eastern/upshear region of Nicholas (Figure 9b). This may have acted to reduce the tilt in the more vigorous cell development and allow for the convective cells to maintain their integrity as they propagated around the eyewall, following Frank & Ritchie (2001). This allows for the bulk of the electrical activity to be shifted counterclockwise into the western eyewall region. However, Corbosiero & Molinari (2002) did point out that the model simulation in Frank & Ritchie was too coarse to resolve this hypothesis in real TCs. They also suggested that deep divergent motion could counteract the TC tilting brought about by strong wind shear (near the eyewall) thereby enhancing electrified convection towards the downshear left region. The CAPE and SRH values progressively decreased for subsequent hourly RAP soundings after 0300 UTC (not shown), indicating that the environment was becoming less favorable for electrification as Nicholas moved north and east (e.g., Figure 3).

Figures 10 and 11 illustrate a dual polarization analysis of the TLE-producing cells for Case I (0240 UTC) and Case III (0250 UTC), respectively. Negative values of Z_{dr} and k_{dp} at altitudes exceeding 15 km (Figure 10 a and 10b) denote vertically oriented ice crystals that are being influenced by a strong electric field (Logan, 2021). This is synonymous with the charge layer altitude presented for Case I (Figure 5). The ρ_{hv} values (<0.95) at that altitude denote a nonhomogeneous size distribution of ice particles. In terms of Case III (Figure 11), there is a larger region of negative Z_{dr} values next to a broad region of positive values which suggests

intense turbulence resulting from the collocated upward and downward motion of the ice particles. The altitude of both Z_{dr} regions is lower than in Case I. In addition, a lower region of negative k_{dp} values is also evident along with a region of ρ_{hv} values less than 0.95. The ρ_{hv} values near 0.95 at 4.5 km can also denote bright banding where the melting of ice crystals to raindrops is likely occurring (Handler & Homeyer, 2018; Logan, 2021). Recall that the mean charge layer altitude in Case III (13.3 km) was found to be lower than Case I (15.2 km).

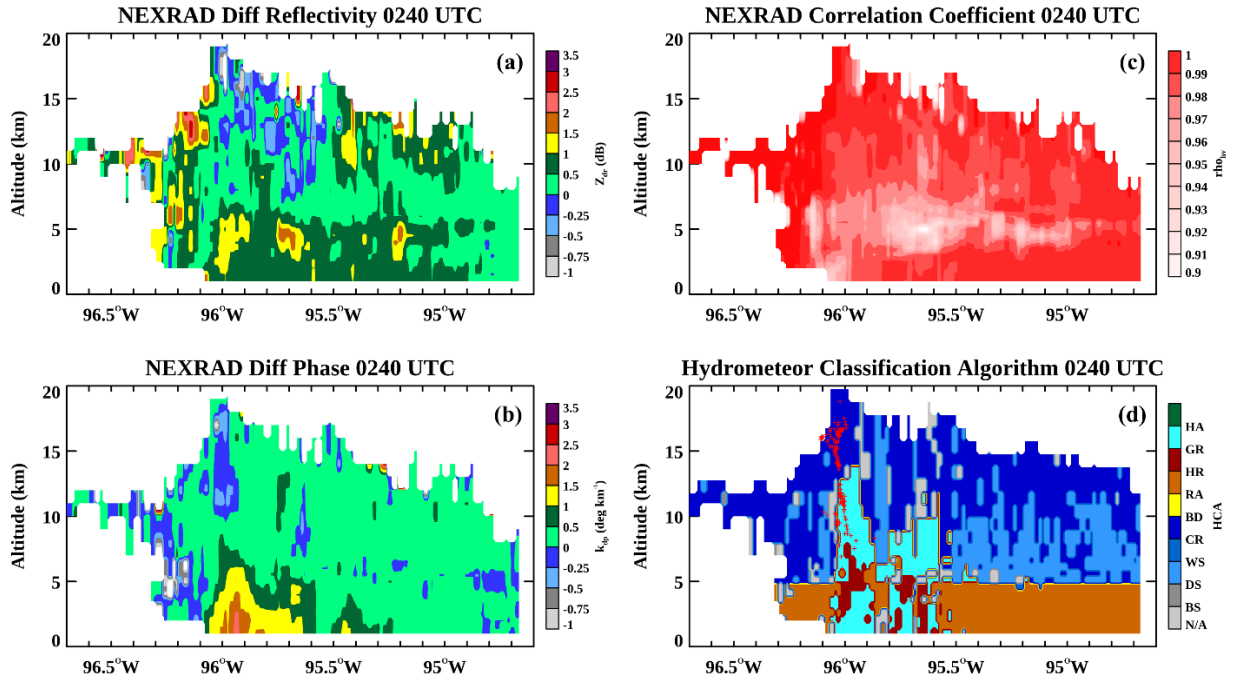

Figure 10. GridRad dual polarization analysis for TLE Case I. (a) Differential reflectivity (Z_{dr}), (b) differential phase (k_{dp}), (c) correlation coefficient (ρ_{hv}), and (d) hydrometeor classification algorithm (HCA) products: biological/chaff particles (BS), dry snow (DS), wet snow (WS), ice crystals (CR), big rain drops (BD), rain (RA), heavy rain (HR), graupel (GR), and hail (HA) (Handler & Homeyer, 2018). The TLE VHF source points (up to 20 km in altitude) are denoted by red pluses.

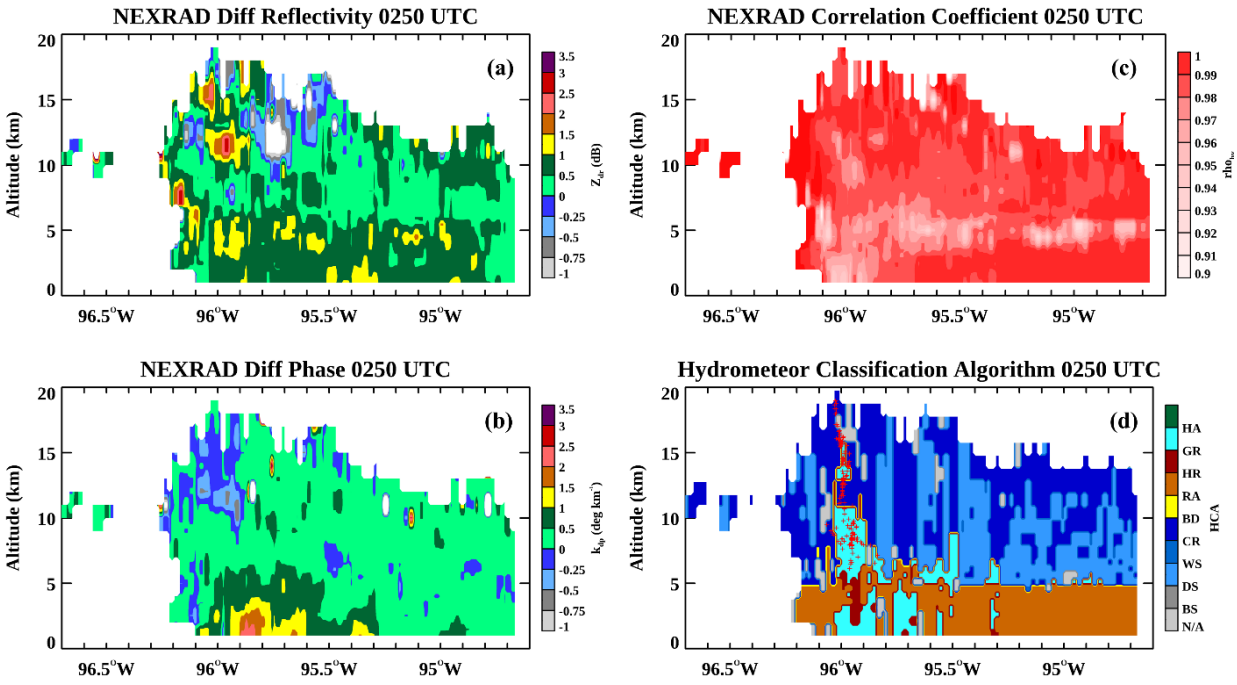

577

578 **Figure 11.** Same as Figure 10 but for TLE Case III.

579 The HCA analysis for Case I (Figure 10d) and Case III (Figure 11d) illustrates the
580 presence of graupel (green feature) at high altitudes, which plays a large microphysical role in
581 cloud electrification. Handler & Homeyer (2018) suggested that during the convective phase of
582 vigorous convection, a graupel "nose" feature can develop and extend to nearly 5 km above the
583 melting level (~4.5 km). Given the intensity of the updraft and observation of TLEs, it is
584 plausible to observe graupel at even higher altitudes, though Handler & Homeyer (2018) pointed
585 out that tropical convection should have lower altitude graupel nose features. The presence of
586 graupel below the melting layer is likely an artifact of GridRad which can misclassify large rain
587 drops as graupel though precipitating small hail cannot be ruled out. Nevertheless, it is evident
588 that other dynamic drivers are at work in the TLE cases, which is explained further.

589 Figure 12 shows a brief progression of strong upper-level divergence (e.g., cloud top
590 detrainment of air parcels) developing in the western eyewall region (denoted by orange "W")

591 between 0240-0250 UTC on 14 September. Radial divergence values exceeding 0.007 s^{-1} were
592 collocated with radar echo top heights exceeding 18 km in the vicinity of the initial TLE VHF
593 source point. This supports the occurrence of vigorous convection and high-altitude lightning
594 activity in the western eyewall region during Case I (Figure 10a). By 0250 UTC, the TLE-
595 producing cell had migrated offshore and featured lower echo top heights (~15 km) as well as
596 lower peak radial divergence values (0.005-0.006 s^{-1}) in the vicinity of the initial TLE VHF
597 source point. Wind vectors backed with height generally implied dry air intrusion (Figures 9b
598 and 9c). Shu et al. (2021) pointed out that this may be an additional reason the upper-level
599 divergence and deep convection strengthened and produced the TLEs. An additional premise to
600 consider is that the TLE producing cell during Case I exhibited the strongest cloud top
601 divergence. The initial cloud top turbulent motions may have aided in eroding the screening
602 charge layer after the Case I and Case II TLEs. The presence of the large positive Z_{dr} region in
603 Case III allowed for some "recharge" for the TLE to reach the highest altitude of all four cases.
604 Afterward, the depletion of the electric field was illustrated by the lowering of Z_{dr}, k_{dp}, and ρ_{hv}
605 altitudes along with the decline in reflectivity values within two radar volume scans which
606 indicated the weakening of the TLE-producing cell after the time of Case III. Moreover, the
607 graupel nose feature lowered and disappeared in the western eyewall region GridRad volume
608 scans after 0300 UTC (not shown). According to Shu et al. (2021), continued dry air intrusion
609 can modulate the vertical precipitation structure and eventually expand the stratiform region,
610 thereby weakening the overall convection over time. This in fact did occur after 0300 UTC when
611 lightning and TLE activity had virtually ended in the eyewall (Supplemental Movie 1).

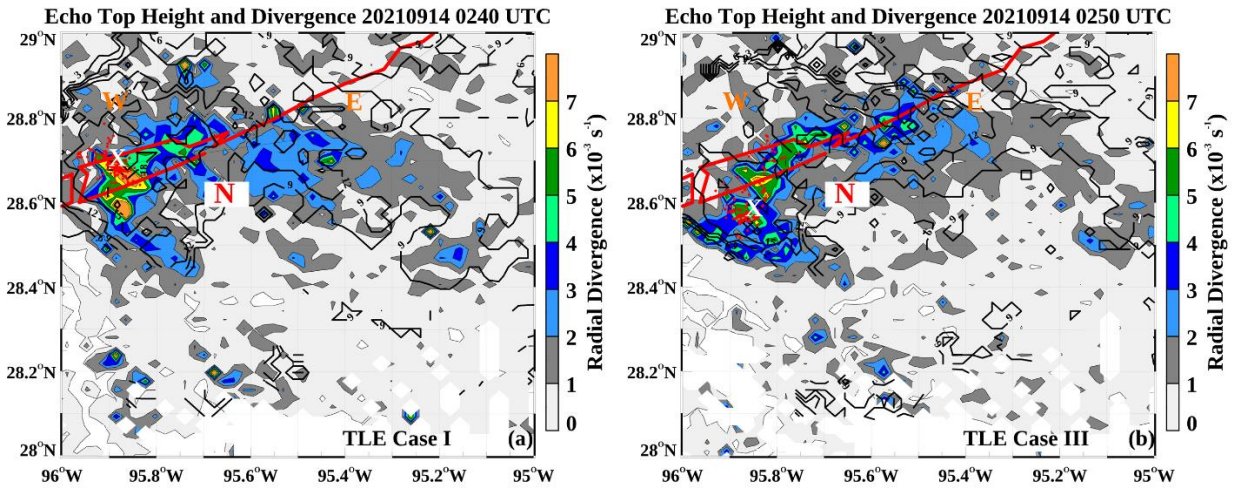

Figure 12. GridRad-derived cloud top height (black line contours denote altitude in kilometers) and radial divergence (color-filled contours) during (a) Case I and (b) Case III. TLE VHF sources are denoted by small red circles and the TLE initiation point by white "X". The center of Nicholas (28.6°N, 95.7°W) during this time is denoted by red "N" and the Texas coastline is denoted in red.

4.2 Charge analysis of the rainband and eyewall

Overall, Nicholas featured a "normal" dipole charge structure with a mixture of inverted dipole and tripole structures. That is, there was a large region of negative charge at 5 km and a small region of negative charge at 10 km which "sandwiched" the dominant positive charge region (9 km) (Figures 1a and 1b). The upper "tail" of the distribution illustrates the contribution of high-altitude sources from the rainband and eyewall convection. At 1900 UTC on 13 September, a robust positive charge region in the rainband developed before the megaflash occurred (Figures 2a and 2b). Due to the distance away from the HLMA centroid, ChargePol could resolve a partial spatial and temporal charge structure of the megaflash (2004 UTC). ChargePol was able to illustrate a developing charge inversion given the lower initial altitude and deep depth of the positive charge region. At 2330 UTC, the positive charge layer ascended to ~15 km indicating the strengthening of the deep convection along the 95°W meridian, extending

630 from a latitude of 28°N up to 28.5°N (Figures 2c and 2d). After Nicholas made landfall there was
631 a return to a predominantly normal charge structure as the lightning activity declined (Figure 2a).

632 The eastern eyewall convection from 0100-0200 UTC on 14 September exhibited a
633 normal dipole structure and was the dominant contributor to the charge time-series and
634 histogram distribution (Figures 3a and 3b). The western eyewall region featured an inverted
635 dipole primarily during the period from 0200-0300 UTC. A low-level negative charge region
636 developed ahead of the upper-level positive charge region at 0230 UTC during the second
637 maximum of VHF source rates (Figure 3a). Moreover, a thin negative charge layer was observed
638 above the positive charge layer at 16 km (Figure 3b). Cases I, III, and IV had the largest
639 contributions of negative VHF sources at that level, while Case II featured a higher number of
640 positive VHF sources. After Nicholas made landfall, eyewall charge structure information was
641 somewhat ambiguous.

642 ChargePol yielded reasonable results regarding charge structures of the tropical deep
643 convection during Nicholas. However, the polarity of the TLEs was not well established because
644 only the positive and negative charge regions from 16 km and downward were primarily
645 resolved by ChargePol. The contribution of VHF sources above 16 km were fewer in comparison
646 and ChargePol is not currently designed to identify the polarity of charge regions above 20 km.
647 Future work will involve using ChargePol in conjunction with manual XLMA charge analysis
648 and incorporating charge moment change and magnetic field analysis to quantify the charge
649 transfer of TLEs to the upper atmosphere during tropical and continental deep convective events
650 in the vicinity of the HLMA.

651

5. Summary

Hurricane Nicholas made landfall along the Texas Gulf Coast at 0530 UTC on 14 September 2021. The Houston Lightning Mapping Array (HLMA) was operational and captured nearly all the lightning activity of Nicholas from 12-14 September 2021. There was appreciable electrified deep convection observed during the TC along with several notable lightning features prior to landfall. Rainband lightning activity sharply increased two hours prior to Nicholas being designated as a Category 1 TC at 0000 UTC 14 September 2021. Between 0100-0300 UTC, eyewall lightning activity became more dominant. By the time Nicholas made landfall, rainband and eyewall deep convection were minimal. Rare lightning events during the TC were observed by the HLMA: (a) an apparent megaflash (linear distance of 220 km) occurred at 2004 UTC on 13 September 2021 in the outermost rainband and appeared to be curved and (b) several jet-like TLEs occurred between 0230-0300 UTC on 14 September 2021 in the western eyewall region.

There was a sharp increase in the rainband VHF source rate prior to Nicholas being upgraded to a Category 1 TC. On the other hand, the VHF source rate was higher in the eyewall along with the mean height of the positive charge region (9 km) compared to the rainband (7 km). This indicates that deep convection was more widespread within the rainband, while the eyewall deep convective cells were more localized and vigorous. The charge structure of Nicholas featured a predominantly normal structure (positive charge region overlying negative charge) with instances of inverted charge (negative charge region overlying a positive region) especially within the eyewall. A low-level (5-7 km) charge inversion was present during the time of the megaflash while an upper-level (15-18 km) charge inversion occurred during the time of the several TLEs.

675 The dynamic and microphysical environment was favorable for observations of the rare
676 lightning events. Two hours before Nicholas was upgraded to a hurricane (2000 UTC 13
677 September 2021), an expansive region of low-level charge developed in the outer rainband
678 region where the megaflash was initiated. The curved nature of the megaflash appeared to follow
679 the cyclonic wind motion of the TC, which suggested a similar advection orientation of not only
680 the hydrometeors responsible for the charge process but of the charge layer in which the
681 megaflash initiated. During the period of 0230-0300 UTC (14 September 2021), additional
682 dynamic enhancements such as backing of upper-level winds with height and strong cloud top
683 radial divergence within the western region of the eyewall acted to (a) enhance collisions
684 between graupel and ice crystals thereby generating a robust upper-level charge layer and (b)
685 erode the upper-level screening charge layer and produce the TLEs. The preferred location of the
686 TLE-producing cell to develop in the western eyewall (left quadrant) rather than the eastern
687 eyewall region (right quadrant) is worth further study to compare and contrast with other TCs
688 passing within the confines of a lightning mapping array.

689 The small-scale spatial and temporal resolution of the HLMA identified several features
690 within the electrified tropical convection of Nicholas that may have been unresolved by other
691 measurement platforms. Hence, lightning mapping arrays are valuable tools to use along with
692 radar and meteorological data in analyzing and discerning the electrified nature of TCs which
693 develop and evolve within their confines. In addition, since ChargePol can output reasonable
694 charge structure data in 4-D, it will be modified and enhanced in future work to examine the
695 spatial and temporal charge structure of electrified deep convection in continental and tropical
696 systems. Though no aerosol loading data was presented in this study, ChargePol along with
697 satellite, surface, and column aerosol measurements will be used to discern the charge structure

of TC electrified cells that develop in clean and polluted environments within the confines of the HLMA.

Acknowledgements

This study combines the results of thesis work performed by Jacob Hale and Sydney Butler. The authors are grateful for the help of Eric Bruning (personal communication and lmatools software package support), Bruno Medina and Lawrence Carey (ChargePol software package support), and Levi Boggs (personal communication for jets and TLEs). The NLDN data were provided by Vaisala, Inc and were requested via their educational data service. The authors are grateful for helpful comments and suggestions from Nick Jones (Anything Weather Communications, Inc). The authors are grateful to Edward Lightbourn (Texas Search and Rescue) for providing ground validation of wind speed measurements as Nicholas made landfall. This study is supported in part by the National Science Foundation (Grant AGS-2019858).

Conflict of Interest

The authors declare no conflicts of interest relevant to this study.

Data Availability Statement

Houston Lightning Mapping Array sensor data are curated and processed by Timothy Logan. The data are available in the Texas Data Repository at https://doi.org/10.18738/T8/6IG8T1. “lmatools” source code is available at https://github.com/deeplycloudy/lmatools. ChargePol

source code is available at https://github.com/brmedin/chargepol. GridRad NEXRAD products are available at https://gridrad.org.

References

Black, R. A., & Hallett, J. (1986). Observations of the distribution of ice in hurricanes. *Journal of the Atmospheric Sciences*, 43(8), 802-822. https://doi.org/10.1175/1520-0469(1986)043<0802:OOTDOI>2.0.CO;2

Boggs, L. D., Liu, N., Riousset, J. A., Shi, F., Lazarus, S., Splitt, M., & Rassoul, H. K. (2018). Thunderstorm charge structures producing gigantic jets. *Scientific Reports*, 8(18085). https://doi.org/10.1038/s41598-018-36309-z

Boggs, L. D., Mach, D., Bruning, E., Liu, N., Van Der Velde, O., Montanyá, J. et al. (2022). Upward propagation of gigantic jets revealed by 3D radio and optical mapping. *Science Advances*, 8(31). https://doi.org/10.1126/sciadv.abl8731

Bruning, E. C., & MacGorman, D. R. (2013). Theory and observations of controls on lightning flash size spectra. *Journal of the Atmospheric Sciences*, 70, 4012-4029. https://doi.org/10.1175/JAS-D-12-0289.1

Carey, L. D., & Rutledge, S. A. (2000). The relationship between precipitation and lightning in tropical island convection: A C-Band Polarimetric Radar Study. *Monthly Weather Review*, 128(8), 2687-2710. https://doi.org/10.1175/1520-0493(2000)128<2687:TRBPAL>2.0.CO;2

Cecil, D. J., & Zipser, E. J. (1999). Relationships between tropical cyclone intensity and satellite-based indicators of inner core convection: 85-GHz ice-scattering signature and lightning. *Monthly Weather Review*, 127, 103–123. https://doi.org/10.1175/1520-0493(1999)127<0103:RBTCIA>2.0.CO;2

Cecil, D. J., Zipser, E. J., & Nesbitt, S. W. (2002). Reflectivity, ice scattering, and lightning characteristics of hurricane eyewalls and rainbands. Part I: Quantitative description. *Monthly Weather Review*, 130, 769–784. https://doi.org/10.1175/1520-0493(2002)130<0769:risalc>2.0.co;2

Chen, S. S., Knaff, J. A., & Marks, F. D., Jr. (2006). Effects of vertical wind shear and storm motion on tropical cyclone rainfall asymmetries deduced from TRMM. *Monthly Weather Review*, 134(11), 3190-3208. https://doi.org/10.1175/MWR3245.1

Chmielewski, V. C., Bruning, E. C., and Ancell, B. C. (2018). Variations of thunderstorm charge structures in West Texas on 4 June 2012. *Journal of Geophysical Research: Atmospheres*, *123*, 9502–9523. https://doi.org/10.1029/2018jd029006

Corbosiero, K. L., & Molinari, J. (2002). The effects of vertical wind shear on the distribution of convection in tropical cyclones. *Monthly Weather Review*, 130(8), 2110–2123. https://doi.org/10.1175/1520-0493(2002)130⟨2110:TEOVWS⟩2.0.CO

Crum, T. D., & Alberty, R. L. (1993). The WSR-88D and the WSR-88D operational support facility. *Bulletin of the American Meteorological Society*, 74(9), 1669–1687. https://doi.org/10.1175/1520-0477(1993)074%3C1669:TWATWO%3E2.0.CO;2

Cullen, M. R. (2013). The Houston Lightning Mapping Array: Network installation and preliminary analysis. Master's Thesis, Texas A & M University. Available electronically from https://hdl.handle.net/969.1/151109

Cummins, K. L., Krider, E. P., & Malone, M. D. (1998). The U.S. National Lightning Detection Network™ and applications of cloud-to-ground lightning data by electric power utilities. *IEEE Transactions on Electromagnetic Compatibility*, 40(4), 465–480. https://doi.org/10.1109/15.736207

DeHart, J. C., & Bell, M. M. (2020). A comparison of the polarimetric radar characteristics of heavy rainfall from Hurricanes Harvey (2017) and Florence (2018). *Journal of Geophysical Research: Atmospheres*, 125. https://doi.org/10.1029/2019jd032212

Didlake, A. C., & Kumjian, M. R. (2017). Examining polarimetric radar observations of bulk microphysical structures and their relation to vortex kinematics in Hurricane Arthur (2014). *Monthly Weather Review*, 145(11), 4521–4541. https://doi.org/10.1175/MWR-D-17-0035.1

Fierro, A. O., Mansell, E. R., Ziegler, C. L., & MacGorman, D. R. (2015). Explicitly simulated electrification and lightning within a tropical cyclone based on the environment of Hurricane Isaac (2012). *Journal of the Atmospheric Sciences*, 72, 4167–4193. https://doi.org/10.1175/jas-d-14-0374.1

Fierro, A. O., & Mansell, E. R. (2017). Electrification and lightning in idealized simulations of a hurricane-like vortex subject to wind shear and sea surface temperature cooling. *Journal of the Atmospheric Sciences*, 74, 2023–2041, https://doi.org/10.1175/JAS-D-16-0270.1

Frank, W. M., & Ritchie E. A. (2001). Effects of vertical wind shear on the intensity and structure of numerically simulated hurricanes. *Monthly Weather Review*, 129, 2249–2269. https://doi.org/10.1175/1520-0493(2001)129<2249:EOVWSO>2.0.CO;2

Fridlind, A. M., van Lier-Walqui, M., Collis, S., Giangrande, S. E., Jackson, R. C., Li, X., et al. (2019). Use of polarimetric radar measurements to constrain simulated convective cell evolution: A pilot study with Lagrangian tracking. *Atmospheric Measurement Techniques*, 12, 2979–3000. https://doi.org/10.5194/amt-12-2979-2019

Fuchs, B. R., Rutledge, S. A., Bruning, E. C., Pierce, J. R., Kodros, J. K., Lang, T. J., et al. (2015). Environmental controls on storm intensity and charge structure in multiple regions of the continental United States. *Journal of Geophysical Research: Atmospheres*, 120, 6575–6596. https://doi.org/10.1002/2015JD023271

Gillett, K. (2024). SounderPy: Vertical Profile Data Retrieval & Analysis Tool for Python (Version 3.0.2). Py-Pi, https://pypi.org/project/sounderpy/

Hallett, J., & Mossop, S. C. (1974). Production of secondary ice particles during the riming process. *Nature*, 249(5452), 26-28.

Han, Y., Luo, H., Wu, Y., Zhang, Y., & Dong, W. (2021). Cloud ice fraction governs lightning rate at a global scale. *Communications Earth and Environment*, 157 (2021). https://doi.org/10.1038/s43247-021-00233-4

Handler, S. L., & Homeyer, C. R. (2018). Radar-Observed Bulk Microphysics of Midlatitude Leading-Line Trailing-Stratiform Mesoscale Convective Systems. *Journal of Applied Meteorology and Climatology*, 57(10), 2231-2248. https://doi.org/10.1175/JAMC-D-18-0030.1

Homeyer, C. R., & Bowman, K. P. (2023). Algorithm description document for version 4.2 of the three-dimensional Gridded NEXRAD WSR-88D Radar (GridRad) dataset. Technical Report.

Homeyer, C. R., Fierro, A. O., Schenkel, B. A., Didlake, A. C., Jr., McFarquhar, G. M., Hu, J. et al. (2021). Polarimetric Signatures in Landfalling Tropical Cyclones. *Monthly Weather Review*, 149(1), 131-154. https://doi.org/10.1175/MWR-D-20-0111.1

Hu, J., Rosenfeld, D., Ryzhkov, A., & Zhang, P. (2020). Synergetic use of the WSR-88D radars, GOES-R satellites, and lightning networks to study microphysical characteristics of hurricanes. *Journal of Applied Meteorology and Climatology*, 59, 1051–1068, https://doi.org/10.1175/jamc-d-19-0122.1

Landsea, C. W. & Franklin, J. L. (2013). Atlantic hurricane database uncertainty and presentation of a new database format. *Monthly Weather Review*, 141, 3576–3592.

Latto, A. S., & Berg, R. (2022). National Hurricane Center Tropical Cyclone Report: Hurricane Nicholas. https://www.nhc.noaa.gov/data/tcr/AL142021_Nicholas.pdf

Leighton, H., Black, R., Zhang, X., Marks, F. D., & Gopalakrishnan, S. G. (2020). Ice particle size distributions from composites of microphysics observations collected in tropical cyclones. *Geophysical Research Letters*, 47. https://doi.org/10.1029/2020GL088762

Liu, N., Spiva, N., Dwyer, J. R., Rassoul, H. K., Free, D., & Cummer, S. (2015). Upward electrical discharges observed above Tropical Depression Dorian. *Nature Communications*, 6 (5995). https://doi.org/10.1038/ncomms6995

Logan, T. (2021). An analysis of the performance of the Houston Lightning Mapping Array during an intense period of convection during Tropical Storm Harvey. *Journal of Geophysical Research: Atmospheres*, 126, e2020JD033270. https://doi.org/10.1029/2020JD033270

Lu, G., Cummer, S. A., Lyons, W. A., Krehbiel, P. R., Li, J., Rison, W., et al. (2011). Lightning development associated with two negative gigantic jets, *Geophysical Research Letters*, 38, L12801, https://doi.org/10.1029/2011GL047662

Lyons, W. A., Bruning, E. C., Warner, T. A., MacGorman, D. R., Edgington, S., Tillier, C., & Mlynarczyk, J. (2020). Megaflashes: Just how long can a lightning discharge get? *Bulletin of the American Meteorological Society*, 101(1), E73–E86. https://doi.org/10.1175/bams-d-19-0033.a

Mecikalski, R. M., Bain, A. L., & Carey, L. D. (2015). Radar and lightning observations of deep moist convection across Northern Alabama during DC3: 21 May 2012. *Monthly Weather Review*, 143(7), 2774-2794. https://doi.org/10.1175/MWR-D-14-00250.1

Medina, B. L., Carey, L. D., Lang, T. J., Bitzer, P. M., Deierling, W., & Zhu, Y. (2021). Characterizing charge structure in Central Argentina thunderstorms during RELAMPAGO utilizing a new charge layer polarity identification method. *Earth and Space Sciences*, 8, e2021EA001803.

Molinari, J., & Vollaro, D. (2010). Distribution of Helicity, CAPE, and Shear in Tropical Cyclones. *Journal of the Atmospheric Sciences*, 67(1), 274-284. https://doi.org/10.1175/2009JAS3090.1

Murphy, M. J., Cramer, J. A., & Said, R. K. (2021). Recent History of Upgrades to the U.S. National Lightning Detection Network. *Journal of Atmospheric and Oceanic Technology*, 38(3), 573-585. https://doi.org/10.1175/JTECH-D-19-0215.1

Pan, B., Wang, Y., Logan, T., Hsieh, J.-S., Jiang, J. H., Li, Y., & Zhang, R. (2020). Determinant role of aerosols from industrial sources in Hurricane Harvey's catastrophe. *Geophysical Research Letters*, 47, e2020GL090014. https://doi.org/10.1029/2020GL090014

Petersen, W. A., & Rutledge, S. A. (2001). Regional variability in tropical convection: Observations from TRMM. *Journal of Climate*, 14, 3566–3586.

Peterson, M., Light, T. E. L., & Shao, X.-M. (2021). Combined optical and radio-frequency measurements of a lightning megaflash by the FORTE satellite. *Journal of Geophysical Research: Atmospheres*, 126(15), e2020JD034411. https://doi.org/10.1029/2020JD034411

Peterson, M. J., Lang, T. J., Logan, T., Wee Kiong, C., Gijben, M., Holle, R., et al. (2022). New WMO certified megaflash lightning extremes for flash distance and duration recorded from space. *Bulletin of the American Meteorological Society*, 103(4), 257–261. https://doi.org/10.1175/bams-d-21-0254.1

Peterson, M. (2023). A survey of thunderstorms that produce megaflashes across the Americas. *Earth and Space Science*, 10, e2023EA002920. https://doi.org/10.1029/2023EA002920

Qu, Z., Korolev, A., Milbrandt, J. A., Heckman, I., Huang, Y., McFarquhar, G. M., Morrison, H., Wolde, M., & Nguyen, C. (2022). The impacts of secondary ice production on microphysics and dynamics in tropical convection. *Atmospheric Chemistry and Physics*, 22, 12287–12310. https://doi.org/10.5194/acp-22-12287-2022

Sandmael, T. N., Homeyer, C. R., Bedka, K. M., Apke, J. M., Mecikalski, J. R., & Khlopenkov, K. (2019). Evaluating the Ability of Remote Sensing Observations to Identify Significantly Severe and Potentially Tornadic Storms. *Journal of Applied Meteorology and Climatology*, 58(12), 2569-2590. https://doi.org/10.1175/JAMC-D-18-0241.1

Schultz, C. J., Carey, L. D., Schultz, E. V., & Blakeslee, R. J. (2015). Insight into the kinematic and microphysical processes that control lightning jumps. *Weather and Forecasting*, 30(6), 1591–1621. https://doi.org/10.1175/waf-d-14-00147.1

Shu, S., Feng, X., & Teng, D. (2021). Observed vertical structure of precipitation influenced by dry air for landfalling tropical cyclones over China. *Journal of Geophysical Research: Atmospheres*, 126, e2020JD034204. https://doi.org/10.1029/2020JD034204

Solorzano, N. N., Thomas, J. N., & Bracy, C. (2018). Monitoring tropical cyclones with lightning and satellite data. *EOS*, 99. https://doi.org/10.1029/2018EO092439

Steiger, S. M., Orville, R. E., & Carey, L. D. (2007). Total lightning signatures of thunderstorm intensity over North Texas. *Monthly Weather Review*, 135, 3281-3302.

Stevenson, S. N., Corbosiero, K. L., & Abarca, S. F. (2016). Lightning in eastern North Pacific tropical cyclones: A Comparison to the North Atlantic. *Monthly Weather Review*, 144(1), 225-239. https://doi.org/10.1175/MWR-D-15-0276.1

Stolz, D. C., Businger, S., & Terpstra, A. (2014). Refining the relationship between lightning and convective rainfall over the ocean. *Journal of Geophysical Research: Atmospheres*, 119, 964-981. https://doi.org/10.1002/2012JD018819

Stolzenburg, M., & Marshall, T. C. (2009). Electric field and charge structure in lightning-producing clouds. *Lightning: Principles, Instruments and Applications*, H.-D. Betz, U. Schumann, P. Laroche (Eds.), Springer, Dordrecht. https://doi.org/10.1007/978-1-4020-9079-0_3

Takahashi, T. (1978). Riming electrification as a charge generation mechanism in thunderstorms. *Journal of the Atmospheric Sciences*, 35, 1536-1548.

Tessendorf, S. A., Rutledge, S. A., & Wiens, K. C. (2007). Radar and lightning observations of normal and inverted polarity multicellular storms from STEPS. *Monthly Weather Review*, 135, 3682-3706.

Thomas, R. J., Krehbiel, P. R., Rison, W., Hunyady, S. J., Winn, W. P., Hamlin, T., & Harlin, J. (2004). Accuracy of the lightning mapping array. *Journal of Geophysical Research*, 109, D14207. https://doi.org/10.1029/2004JD004549

Wang, F., Liu, H., Dong, W., Zhang, Y., & Meng, Q. (2018). Characteristics of lightning flashes associated with the charge layer near the 0 °C isotherm in the stratiform region of mesoscale convective systems. *Journal of Geophysical Research: Atmospheres*, 123, 9524–9541. https://doi.org/10.1029/2018JD028569

Wang, Y., Lu, G., Peng, K.-M., Ma, M., Cummer, S. A., Chen, A. B., & Zhu, B. (2021). Space-based observation of a negative sprite with an unusual signature of associated sprite current. *Journal of Geophysical Research: Atmospheres*, 126, e2020JD033686. https://doi.org/10.1029/2020JD033686

Weiss, S. A., MacGorman, D. R., Bruning, E. C., & Chmielewski, V. C. (2018). Two Methods for Correcting Range-Dependent Limitations of Lightning Mapping Arrays. *Journal of Atmospheric and Oceanic Technology*, 35(6), 1273-1282. https://doi.org/10.1175/JTECH-D-17-0213.1

Wiens, K. C., Rutledge, S. A., & Tessendorf, S. A. (2005). The 29 June 2000 supercell observed during STEPS. Part II: Lightning and charge Structure. *Journal of the Atmospheric Sciences*, 62, 4151-4177.

Williams, E. R. (1985). Large-scale charge separation in thunderclouds. *Journal of Geophysical Research*, 90(D4), 6013–6025. https://doi.org/10.1029/JD090iD04p06013

Wood, K. M., & Ritchie, E. A. (2015). A definition for rapid weakening of North Atlantic and eastern North Pacific tropical cyclones. *Geophysical Research Letters*, 42, 10,091–10,097. https://doi.org/10.1002/2015GL066697

Xu, W., Rutledge, S. A., & Zhang, W. (2017). Relationships between total lightning, deep convection, and tropical cyclone intensity change. *Journal of Geophysical Research: Atmospheres*, 122, 7047–7063. https://doi.org/10.1002/2017JD027072

Figure 1.

Hurricane Nicholas 12-14 September 2021

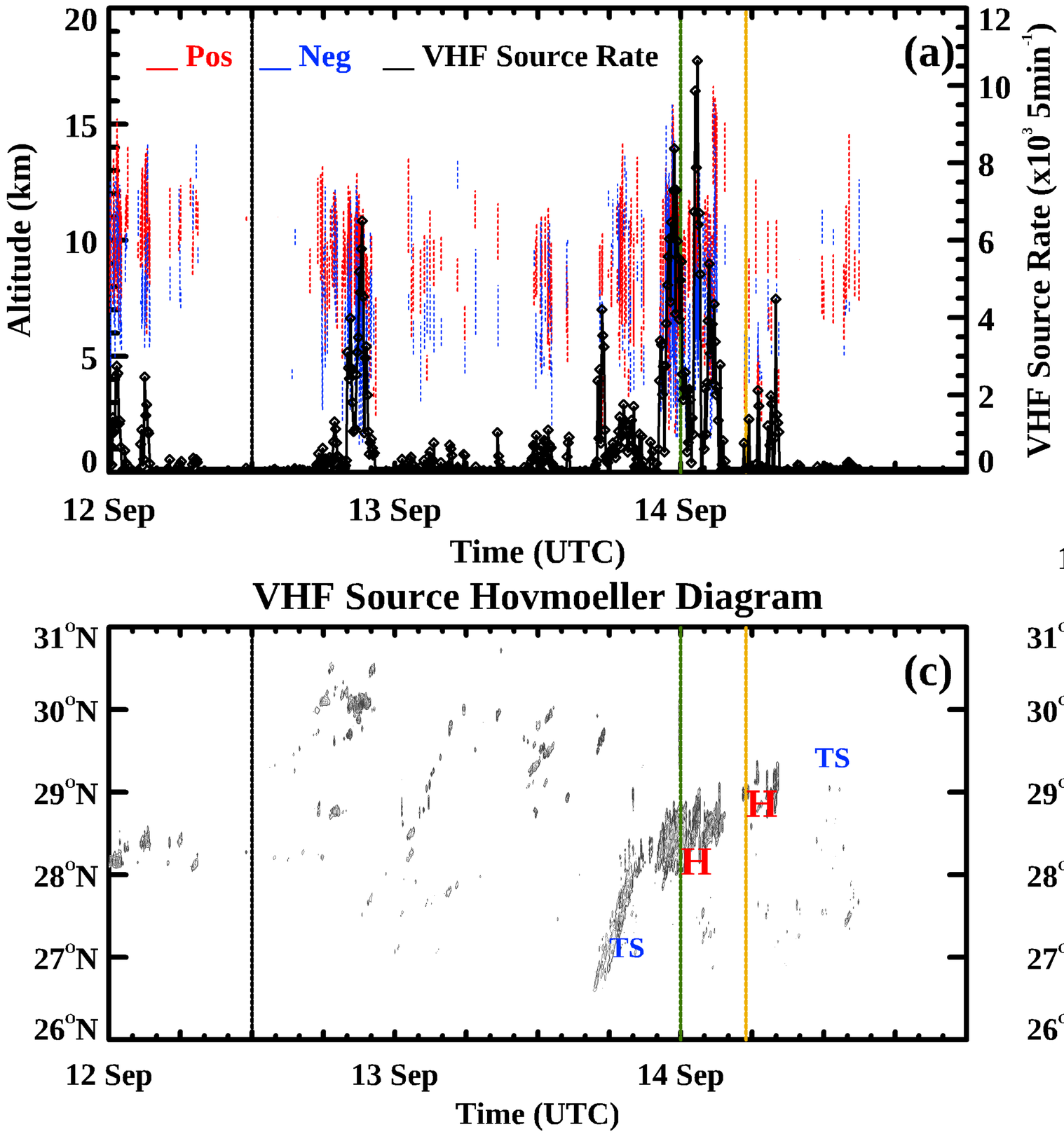

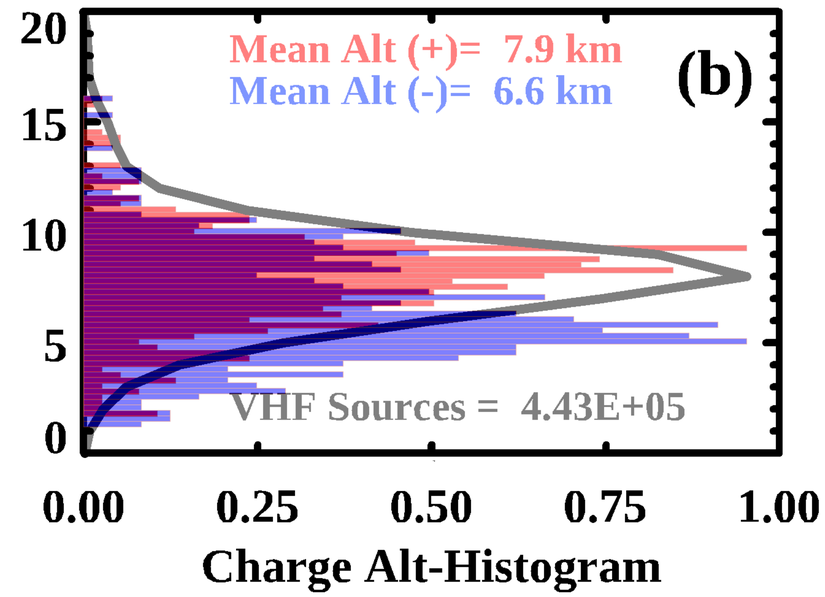

XLMA Figure

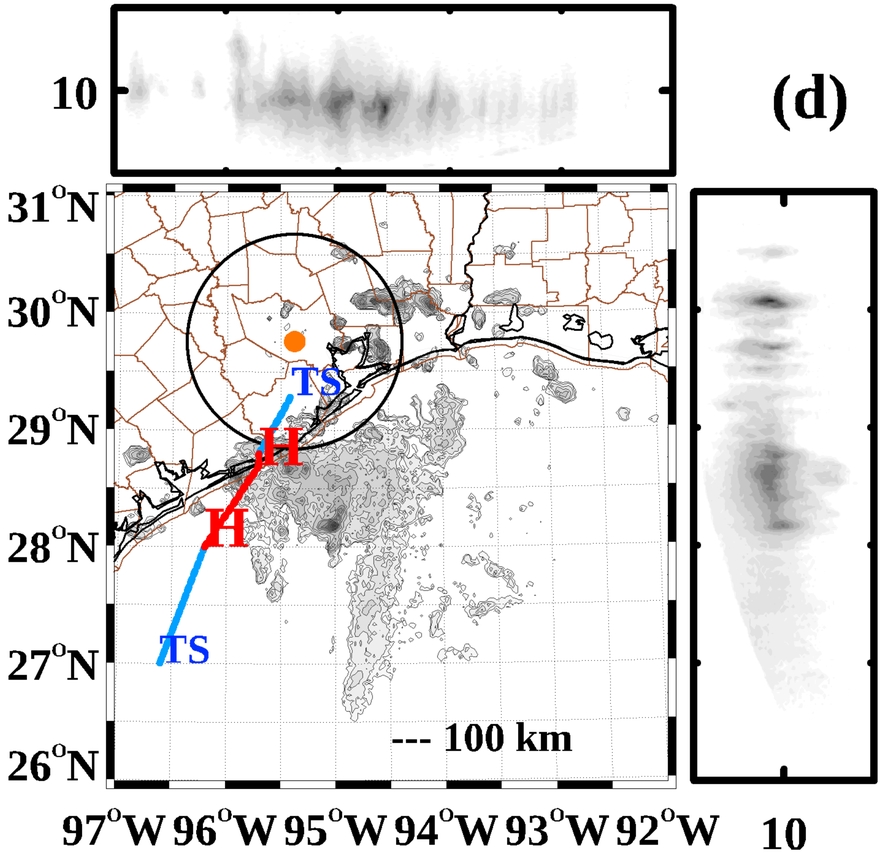

Figure 2.

Hurricane Nicholas Rainband 13-14 September 2021

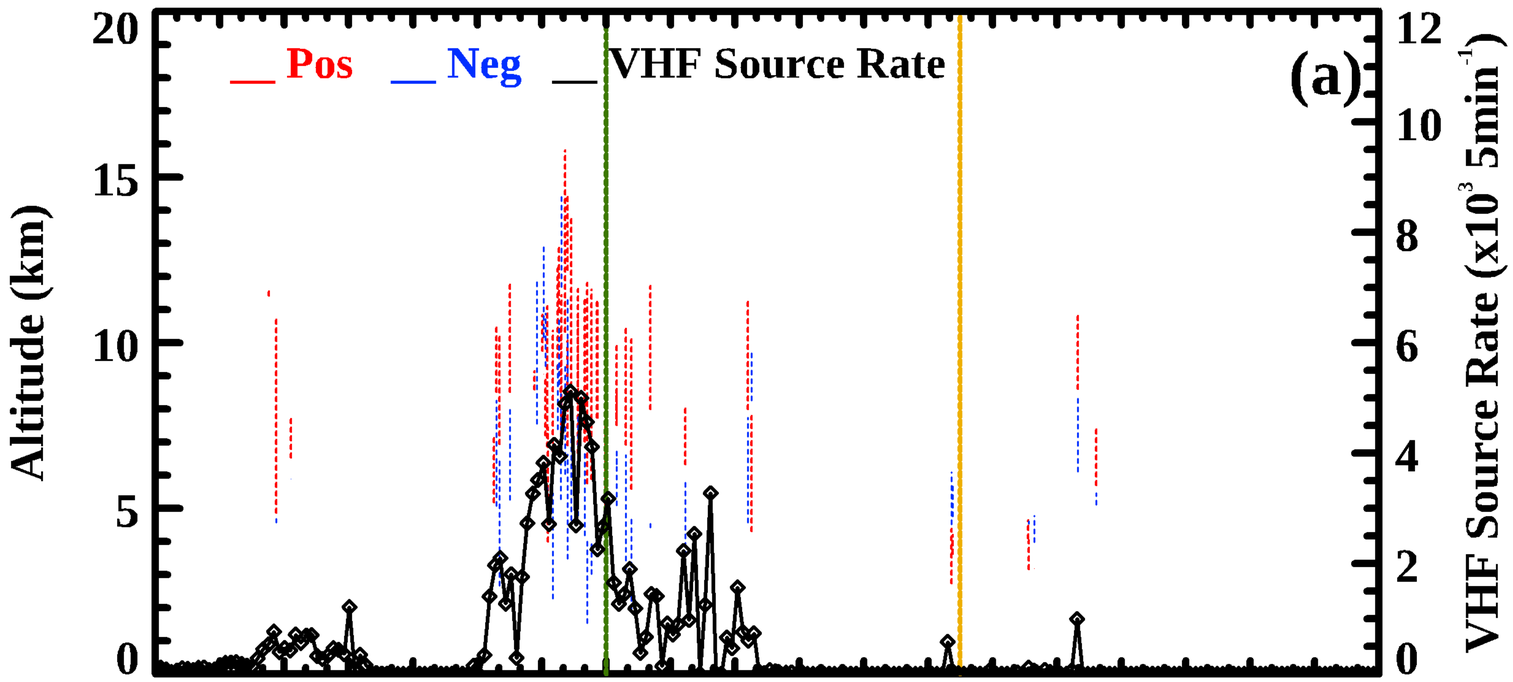

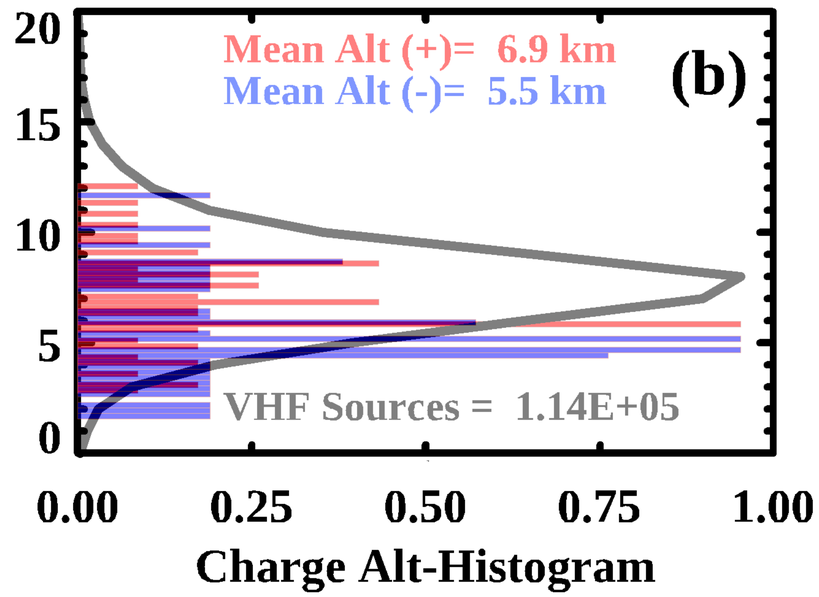

XLMA Figure

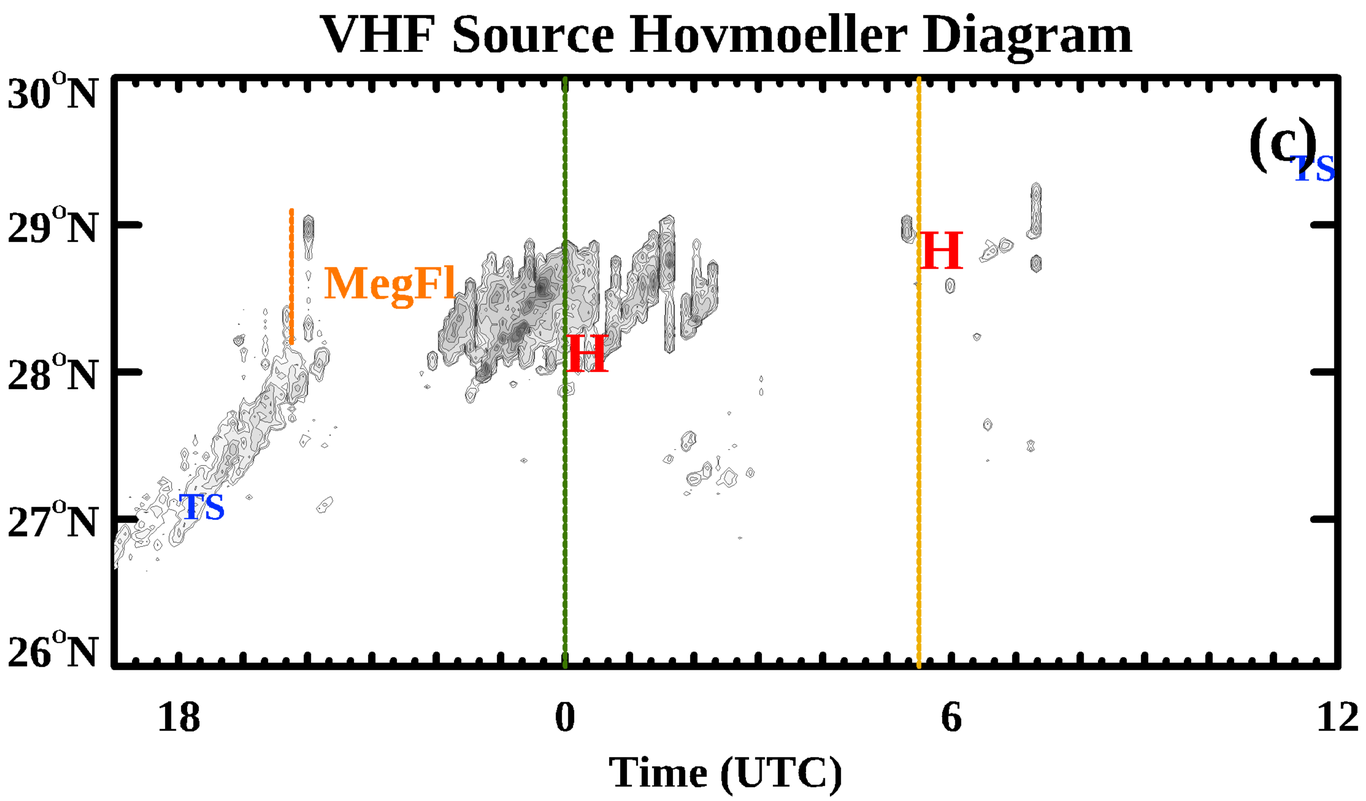

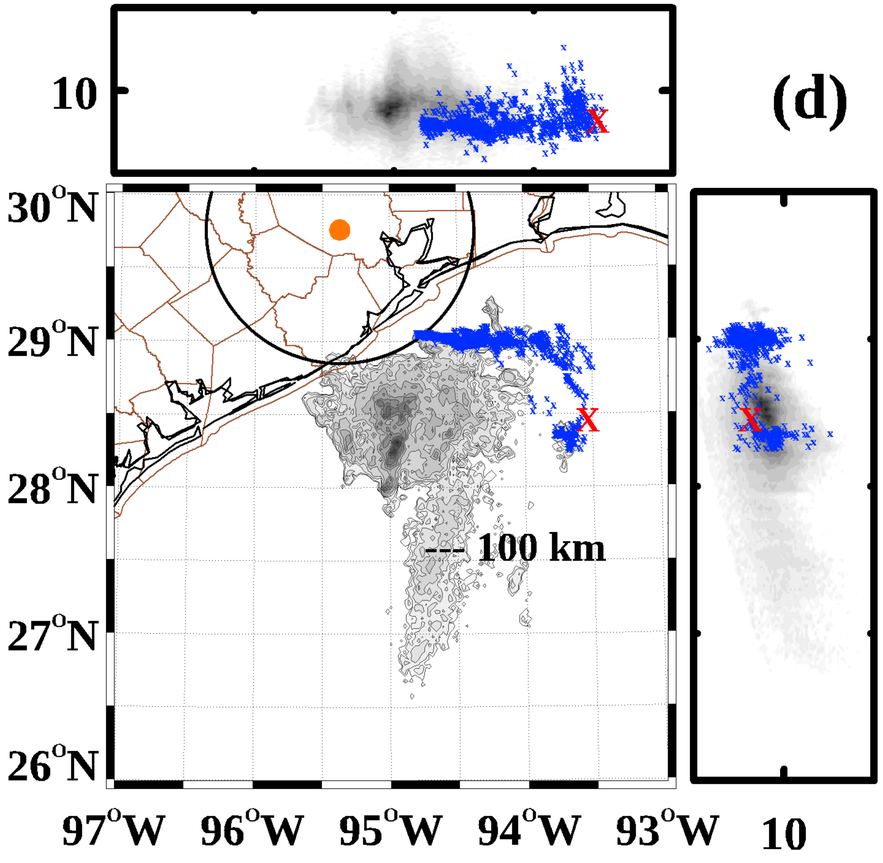

Figure 3.

Hurricane Nicholas Eyewall 13-14 September 2021

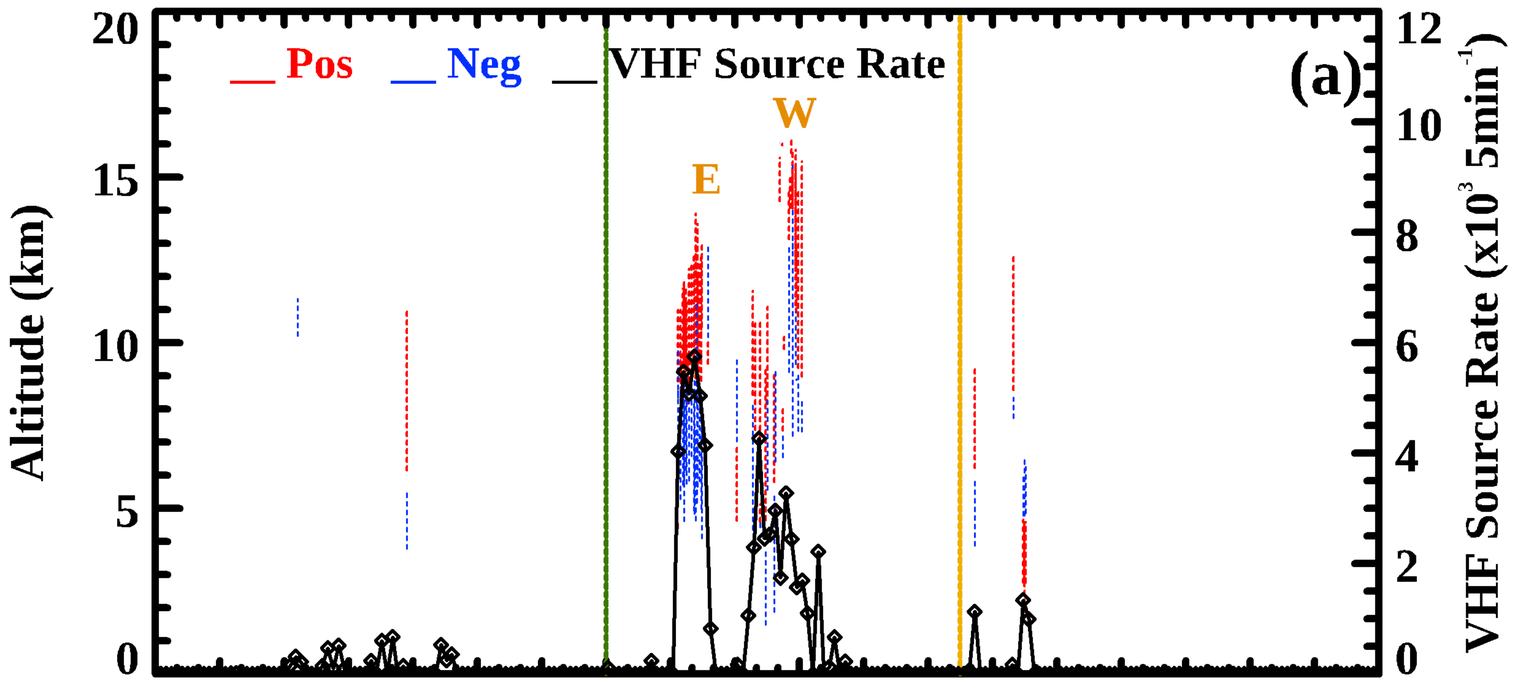

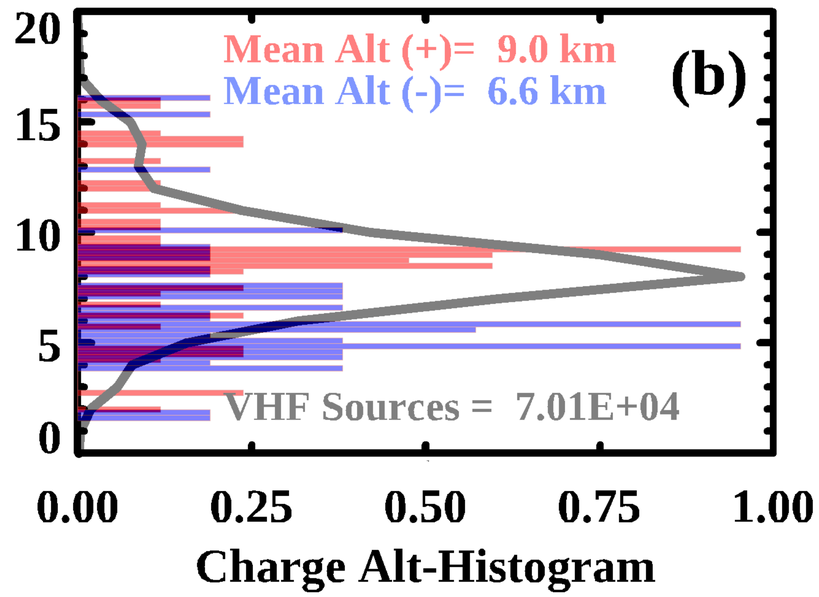

XLMA Figure

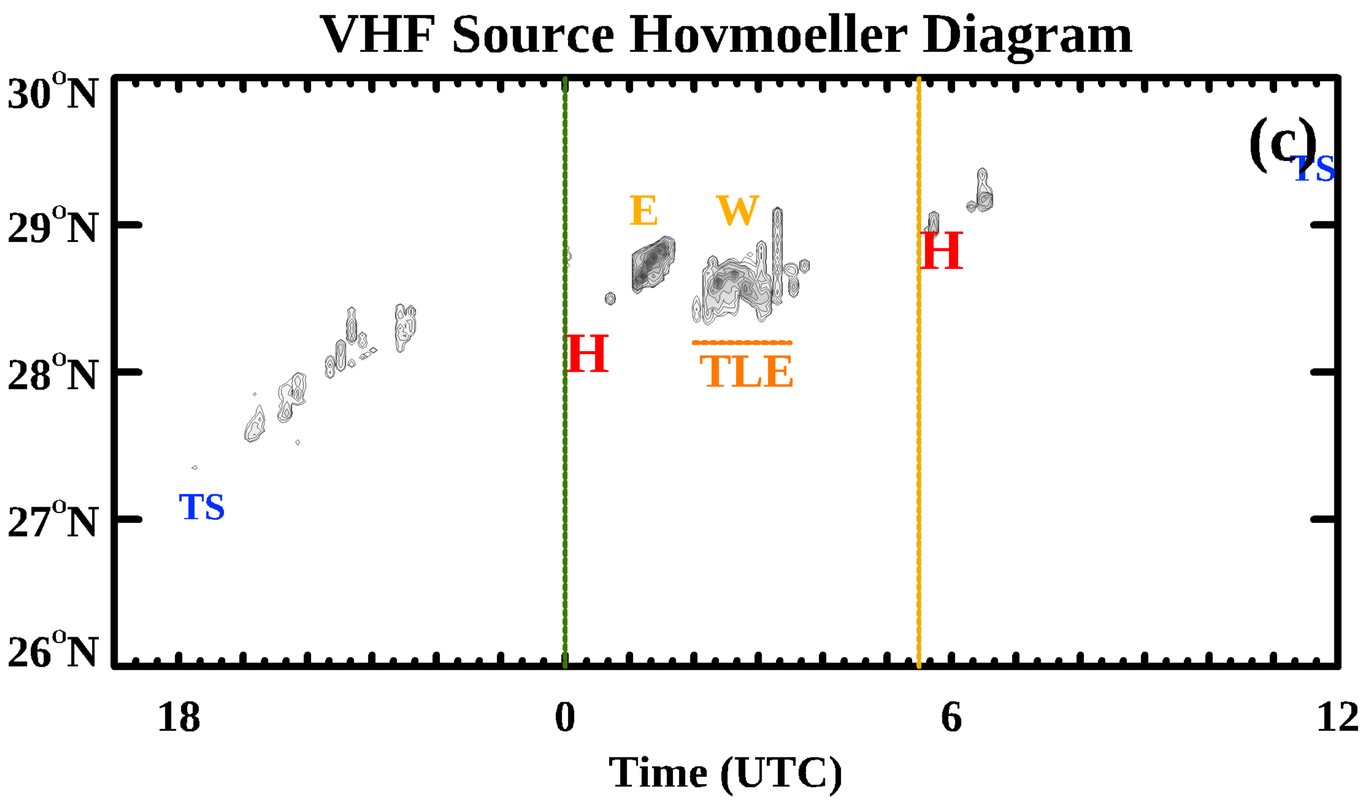

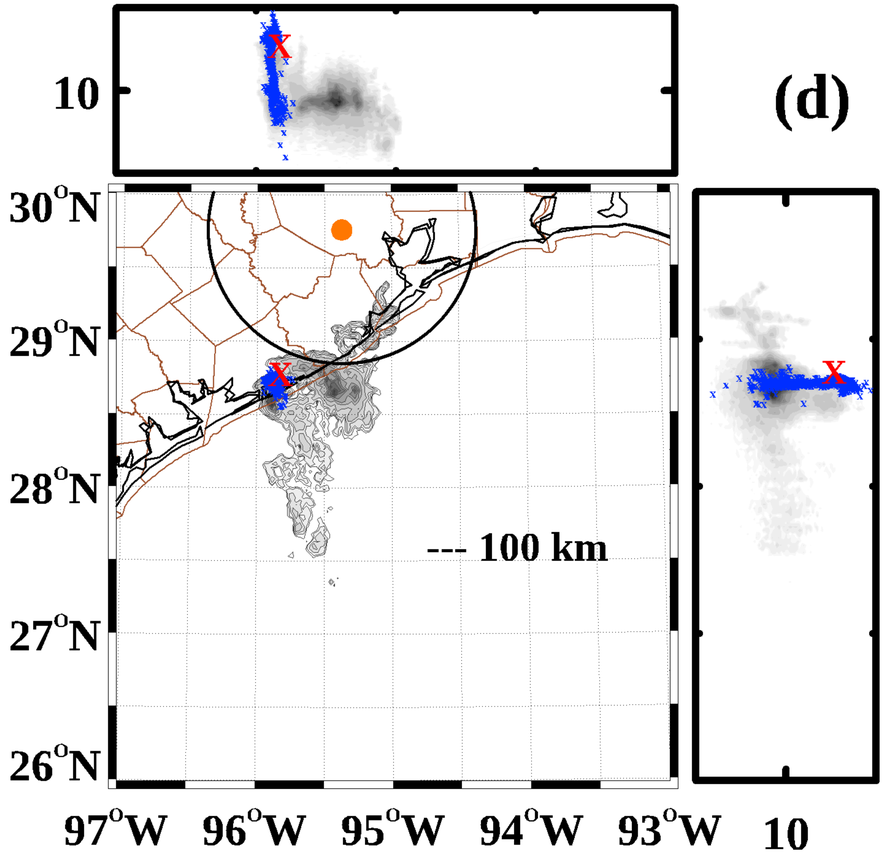

Figure 4.

Hurricane Nicholas Megaflash Case

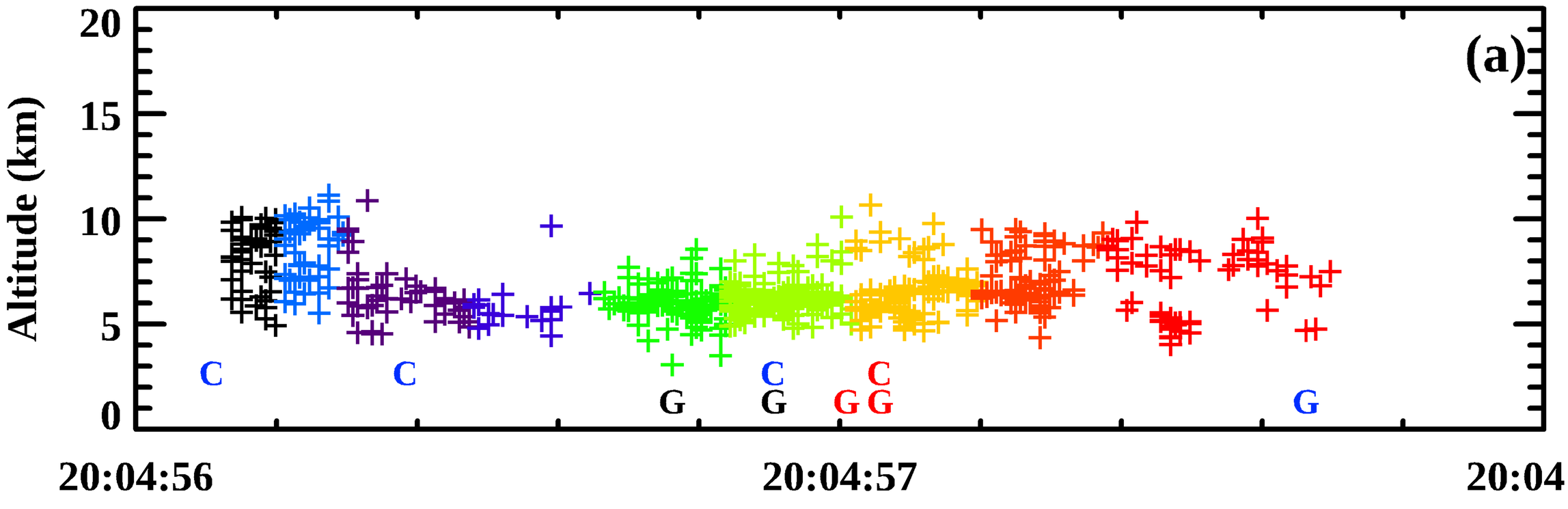

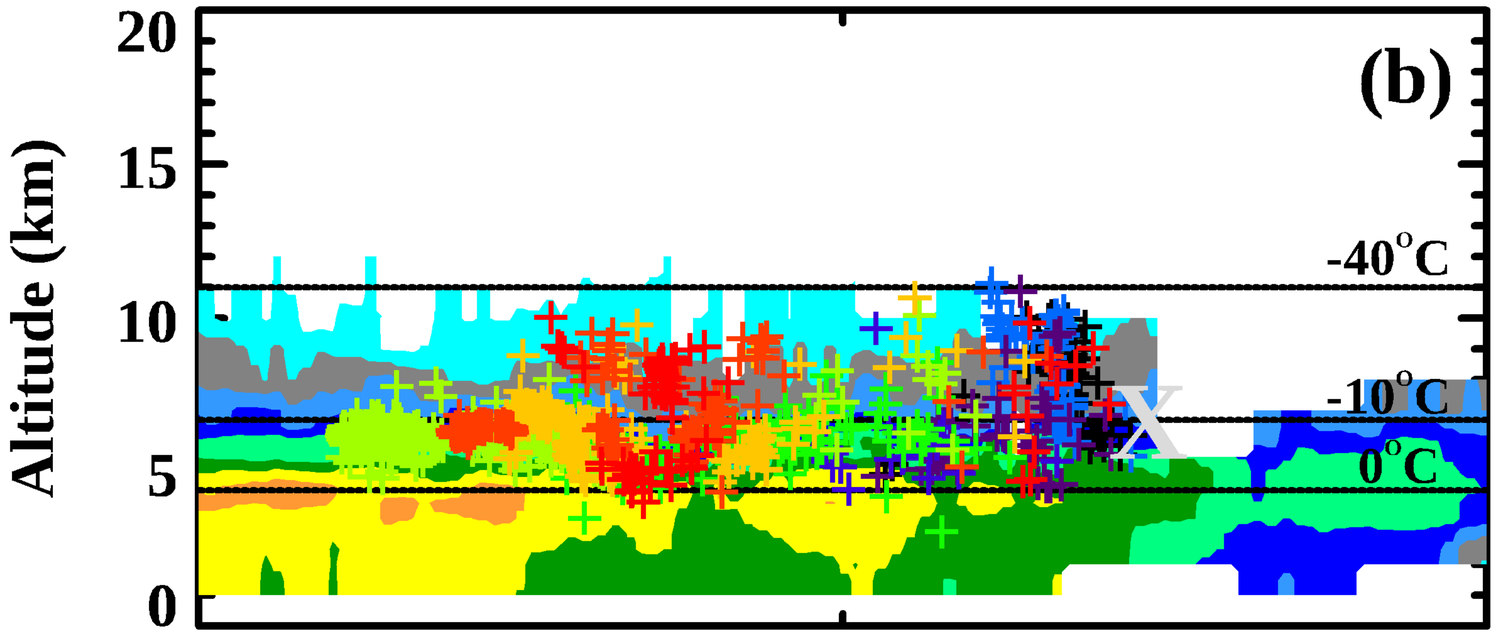

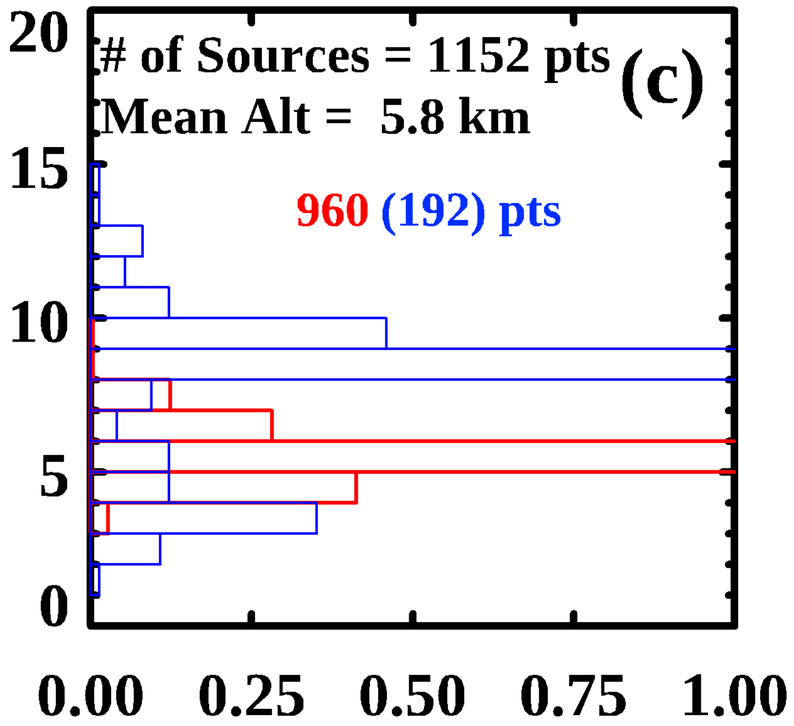

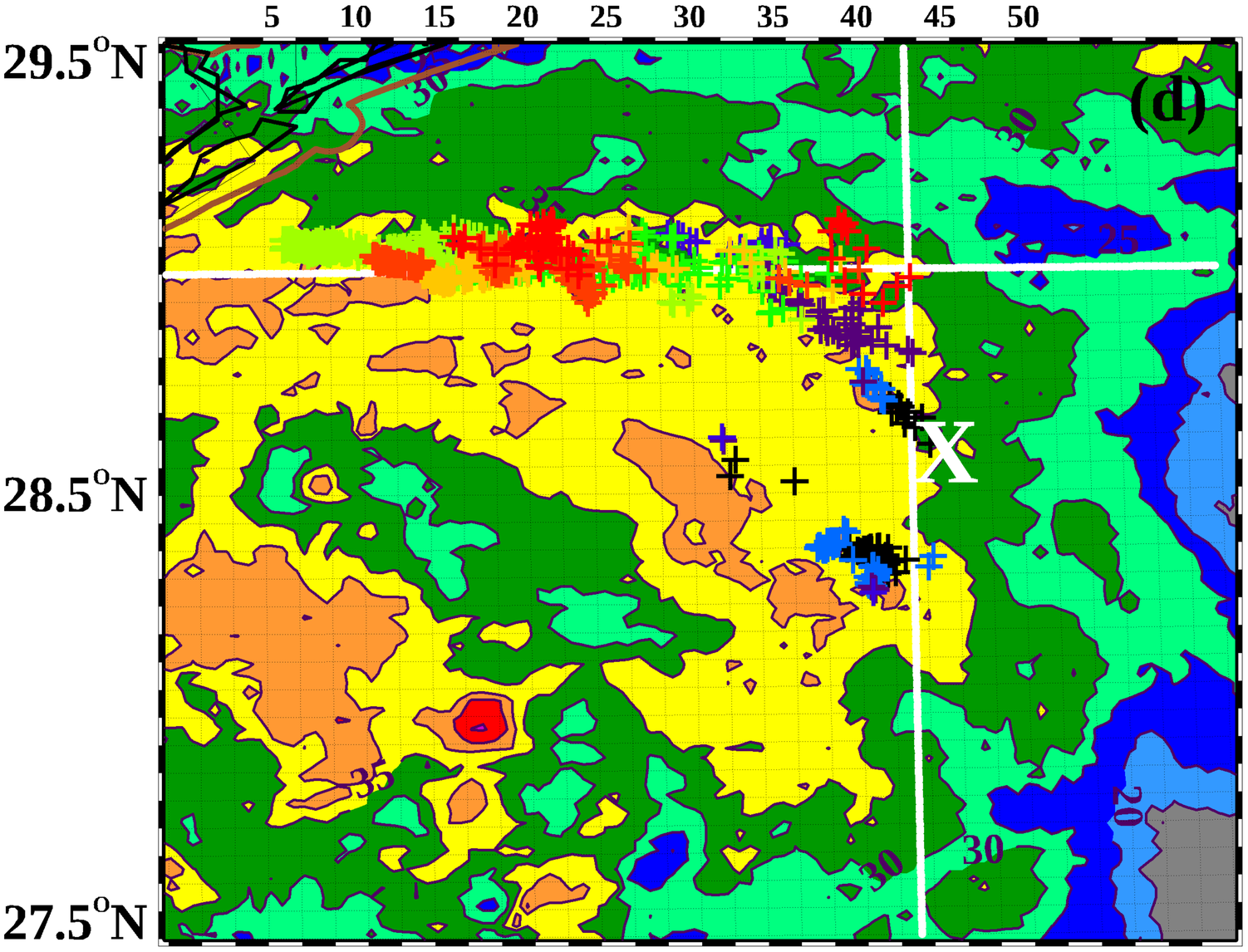

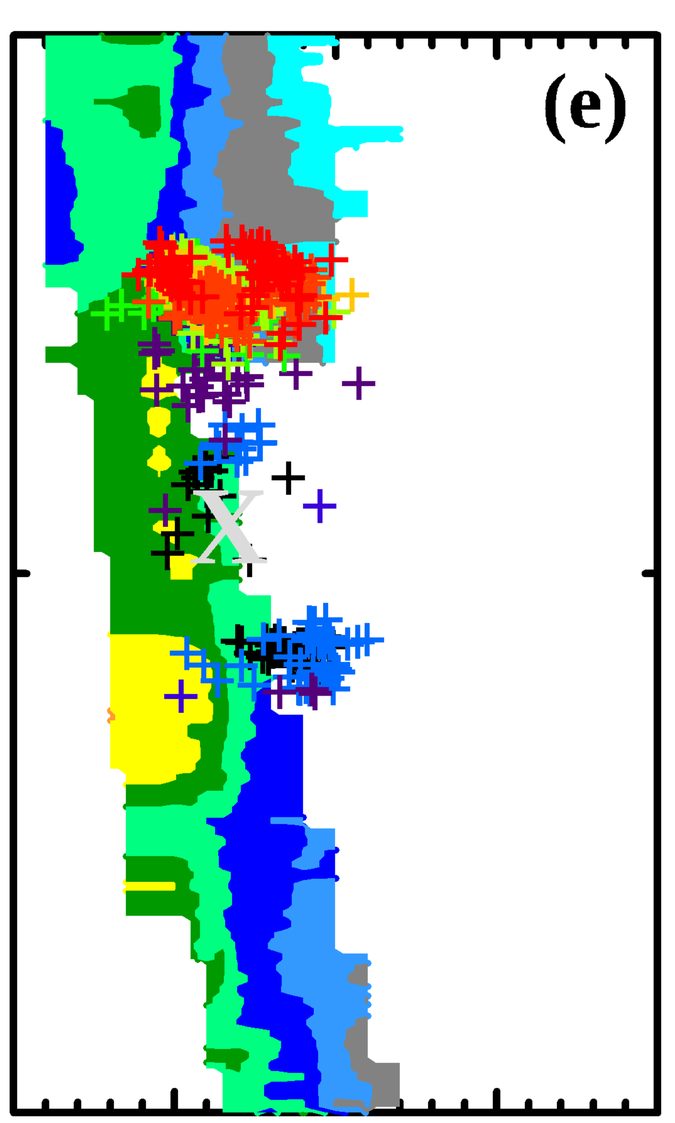

Figure 5.

Hurricane Nicholas TLE Case I

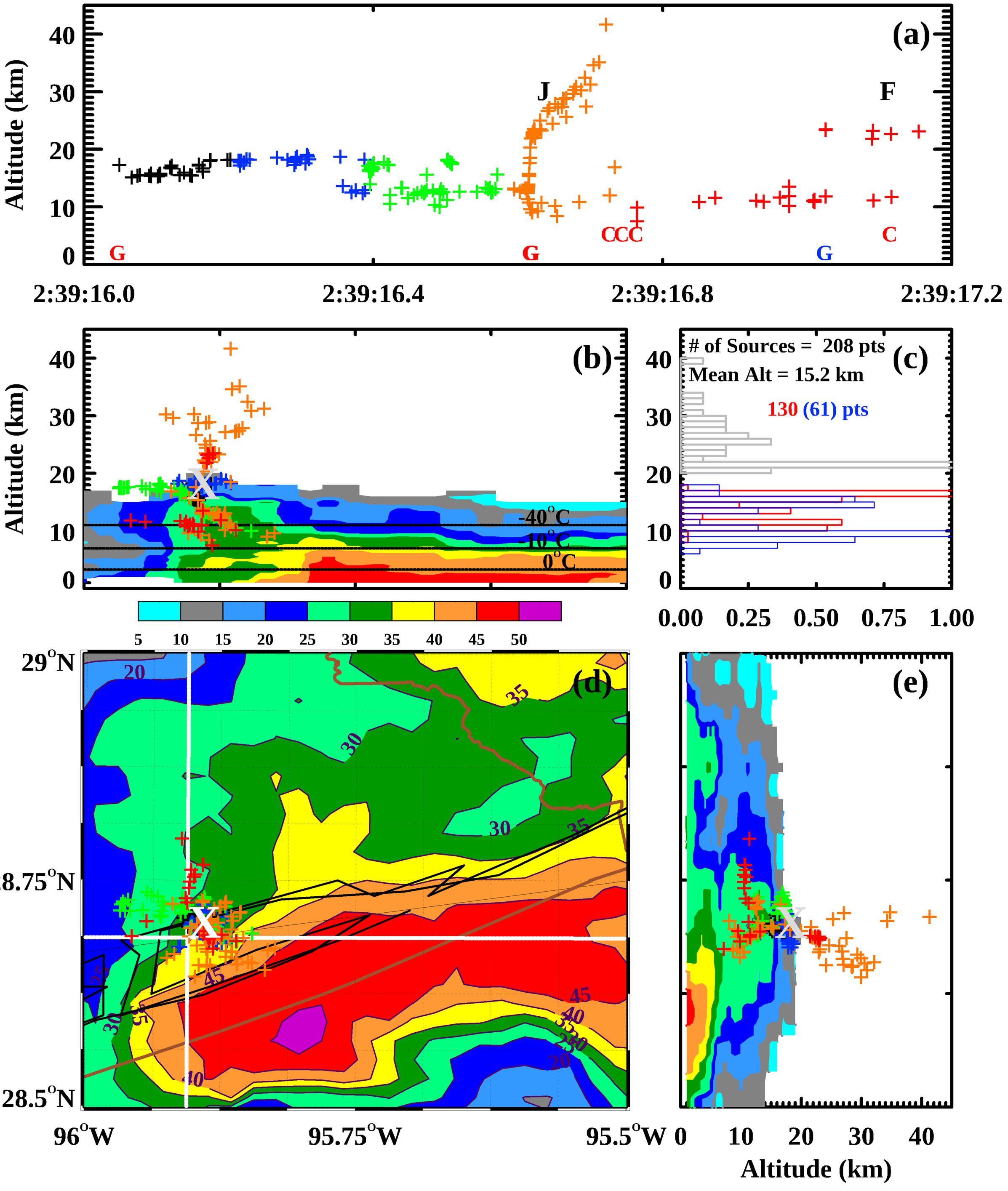

Figure 6.

Hurricane Nicholas TLE Case II

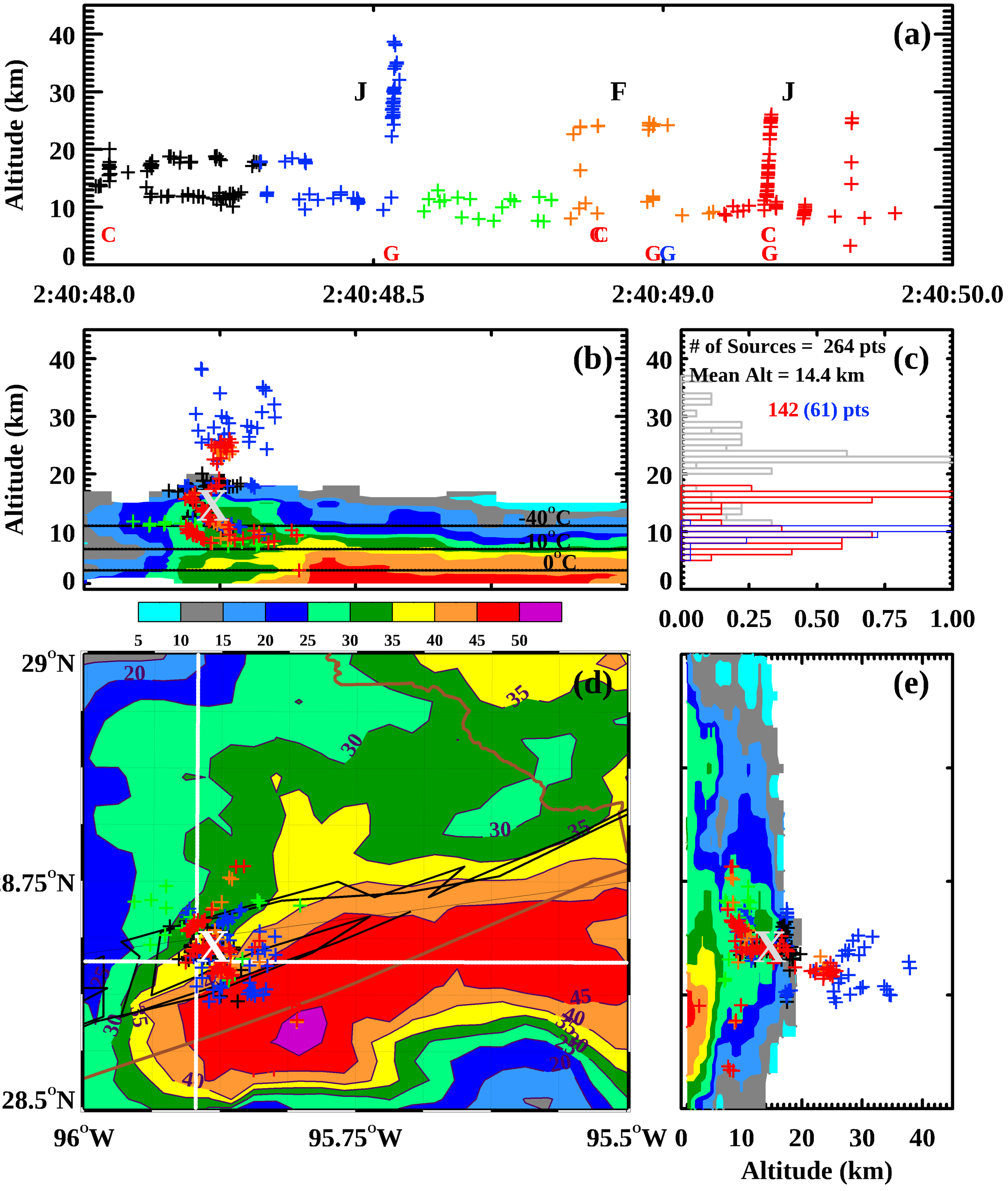

Figure 7.

Hurricane Nicholas TLE Case III

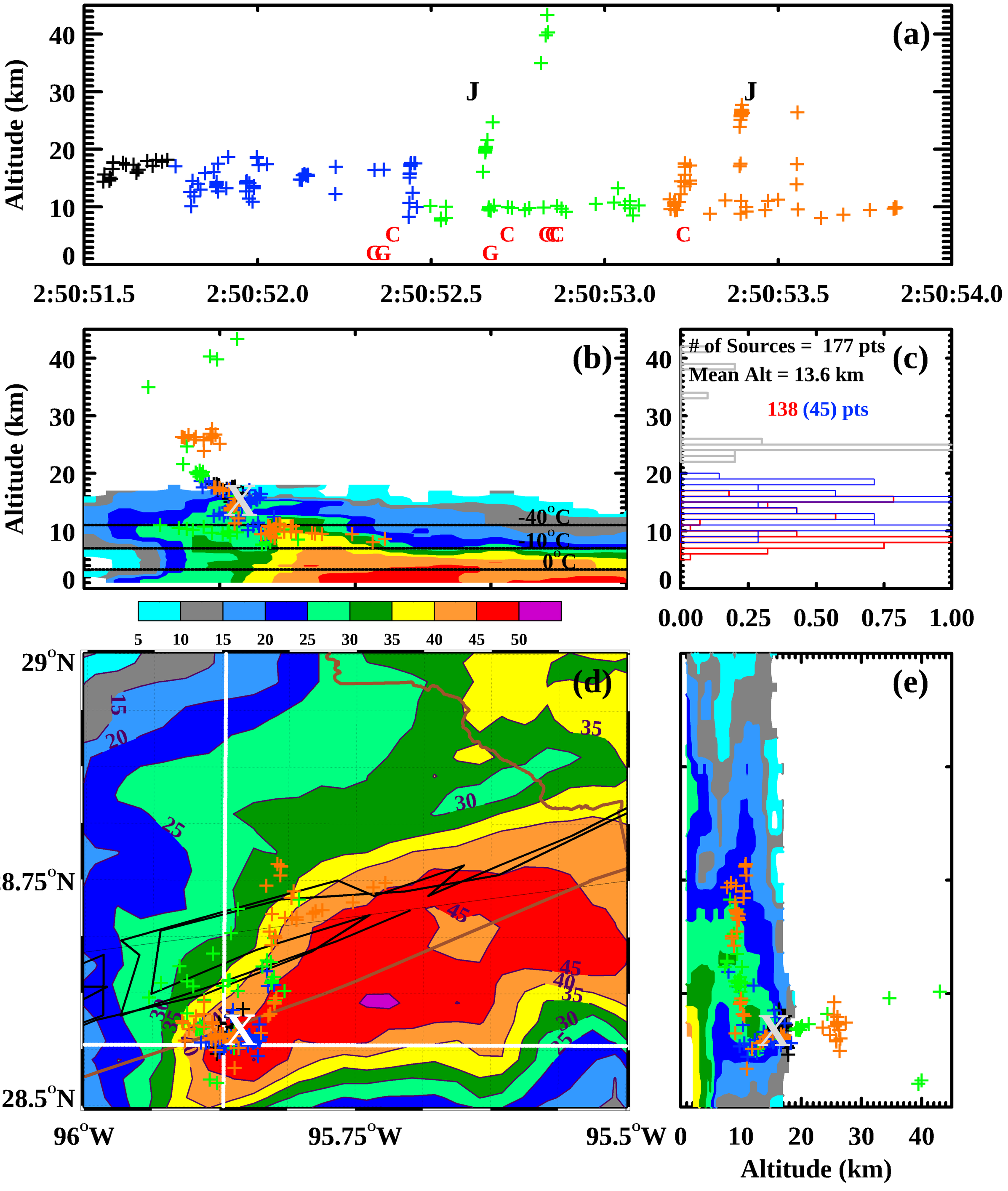

Figure 8.

Hurricane Nicholas TLE Case IV

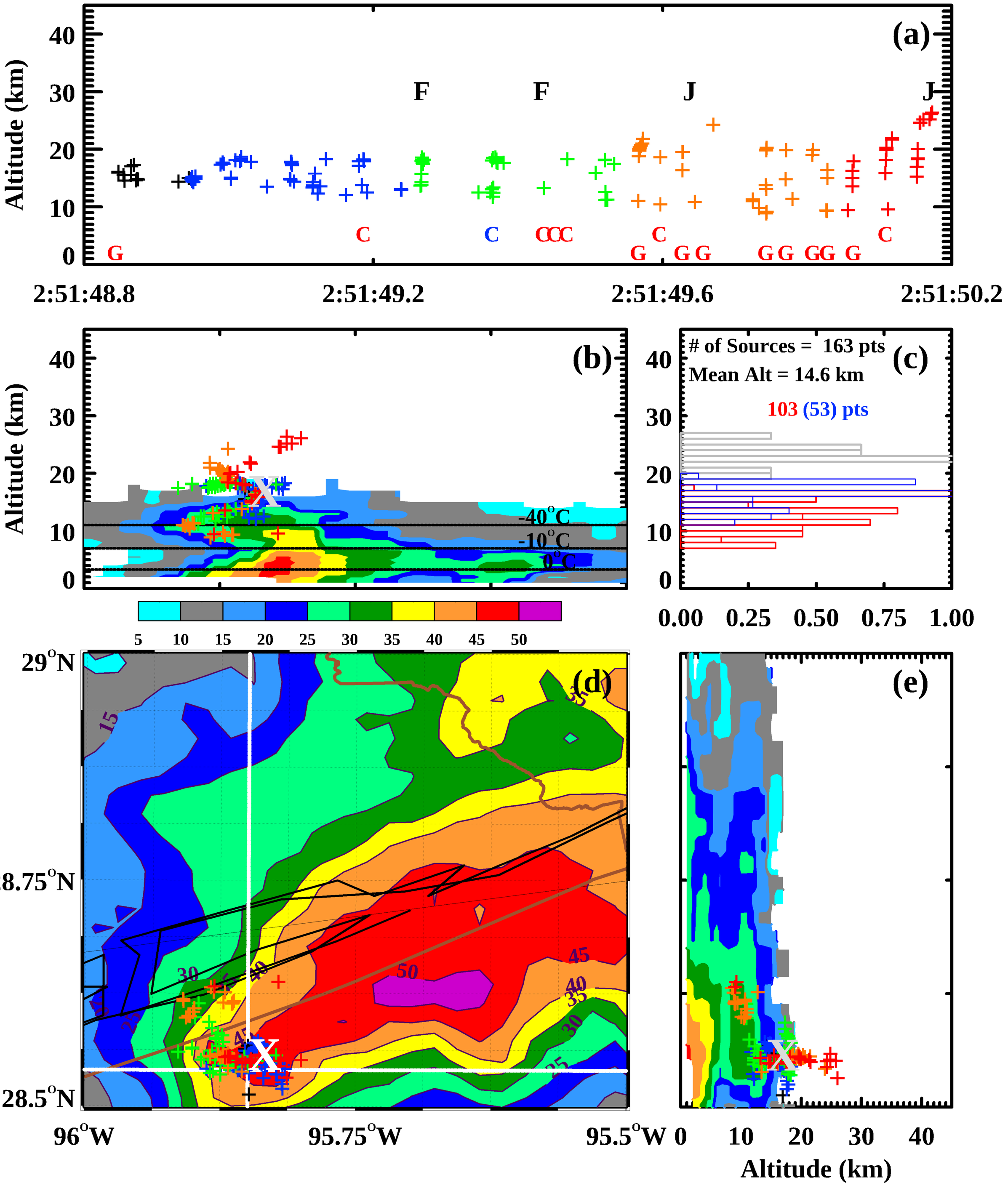

Figure 9.

MODEL REANALYSIS VERTICAL PROFILE | 20Z RAP F00

20Z RAP F00 | VALID: 09/13/2021 20Z

28.5, -93.5 | 0.1° BOX AVG

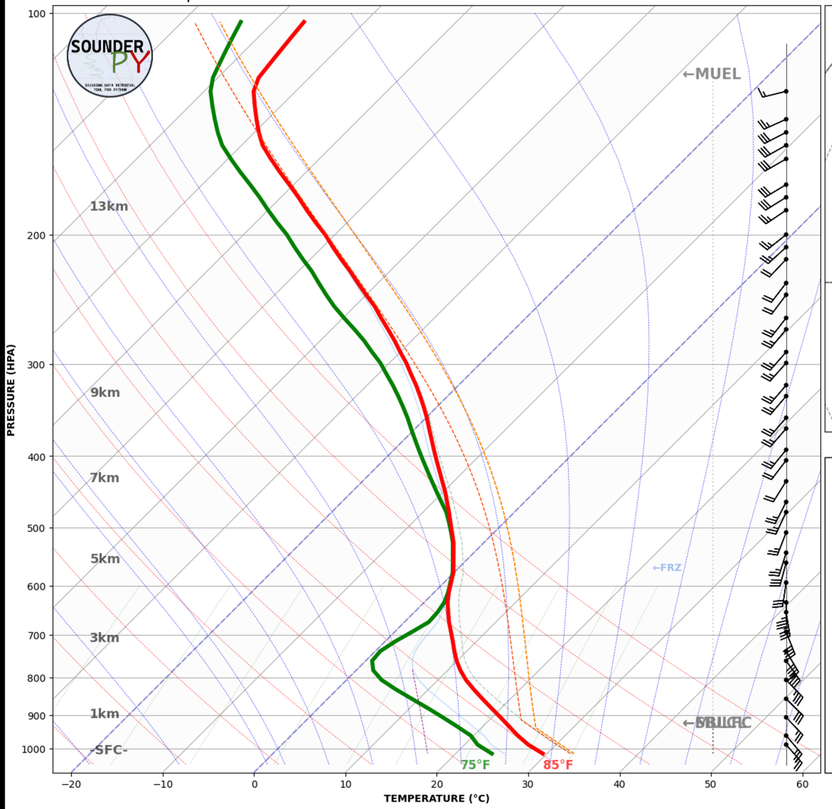

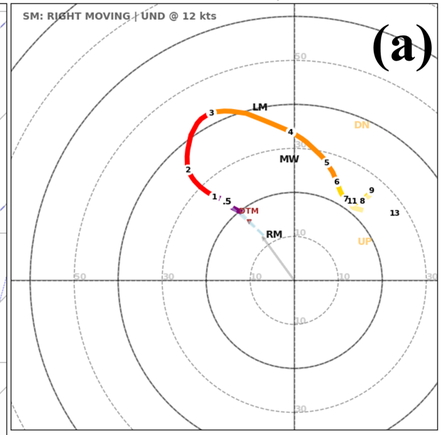

SBCAPE:	2445 J/kg	0-500m SRH:	0 m²/s²
SBCIN:	0 J/kg	0-500m SHEAR:	3 kts
MLCAPE:	1112 J/kg	0-1km SRH:	-3 m²/s²
MLCIN:	-1 J/kg	0-1km SHEAR:	6 kts
MUCAPE:	2445 J/kg	1-3km SRH:	97 m²/s²
MUCIN:	0 J/kg	1-3km SHEAR:	19 kts
3km MUCAPE:	367	3-6km SRH:	219 m²/s²
DCAPE:	629	3-6km SHEAR:	32 kts
ECAPE:	1243 J/kg	0-500m SWV:	23 %

SOUNDERPY VERTICAL PROFILE ANALYSIS TOOL | (C) KYLE J GILLETT

MODEL REANALYSIS VERTICAL PROFILE | 02Z RAP F00

02Z RAP F00 | VALID: 09/14/2021 02Z

28.6, -95.9 | 0.1° BOX AVG

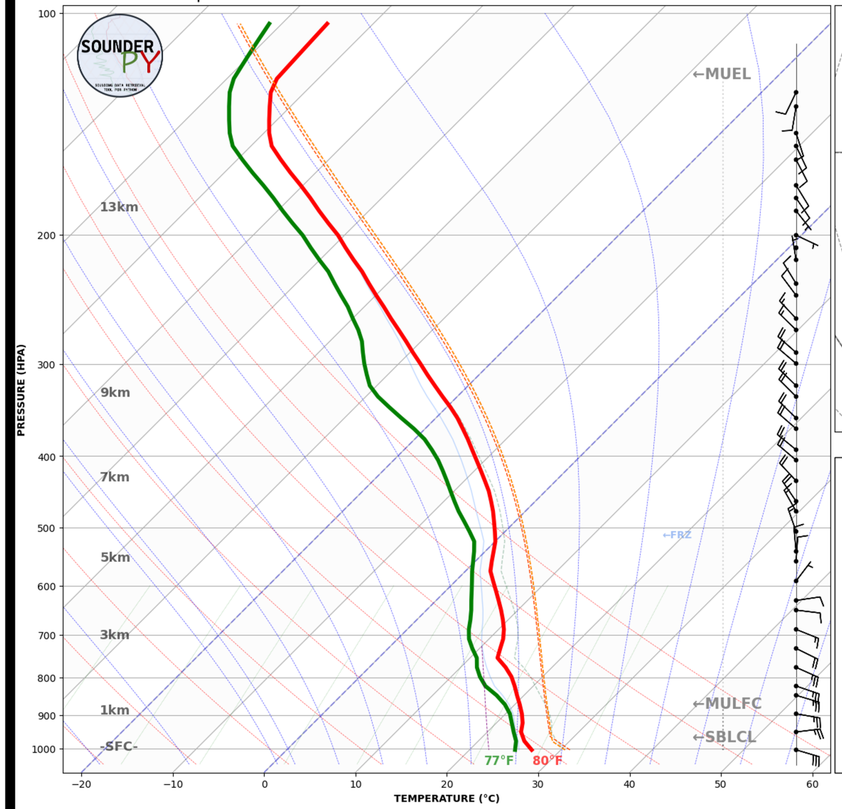

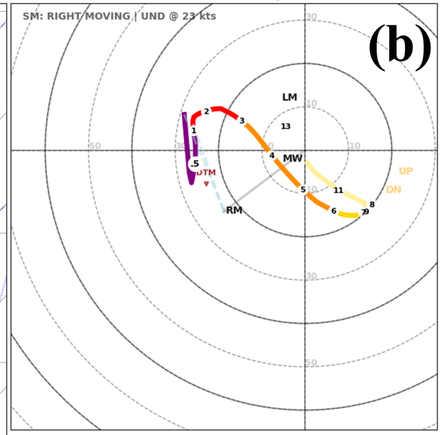

SBCAPE:	1793 J/kg	0-500m SRH:	-19 m²/s²
SBCIN:	-7 J/kg	0-500m SHEAR:	11 kts
MLCAPE:	1628 J/kg	0-1km SRH:	-7 m²/s²
MLCIN:	-9 J/kg	0-1km SHEAR:	4 kts
MUCAPE:	1793 J/kg	1-3km SRH:	76 m²/s²
MUCIN:	-7 J/kg	1-3km SHEAR:	11 kts
3km MUCAPE:	102	3-6km SRH:	126 m²/s²
DCAPE:	309	3-6km SHEAR:	29 kts
ECAPE:	1500 J/kg	0-500m SWV:	53 %

SOUNDERPY VERTICAL PROFILE ANALYSIS TOOL | (C) KYLE J GILLETT

Figure 10.

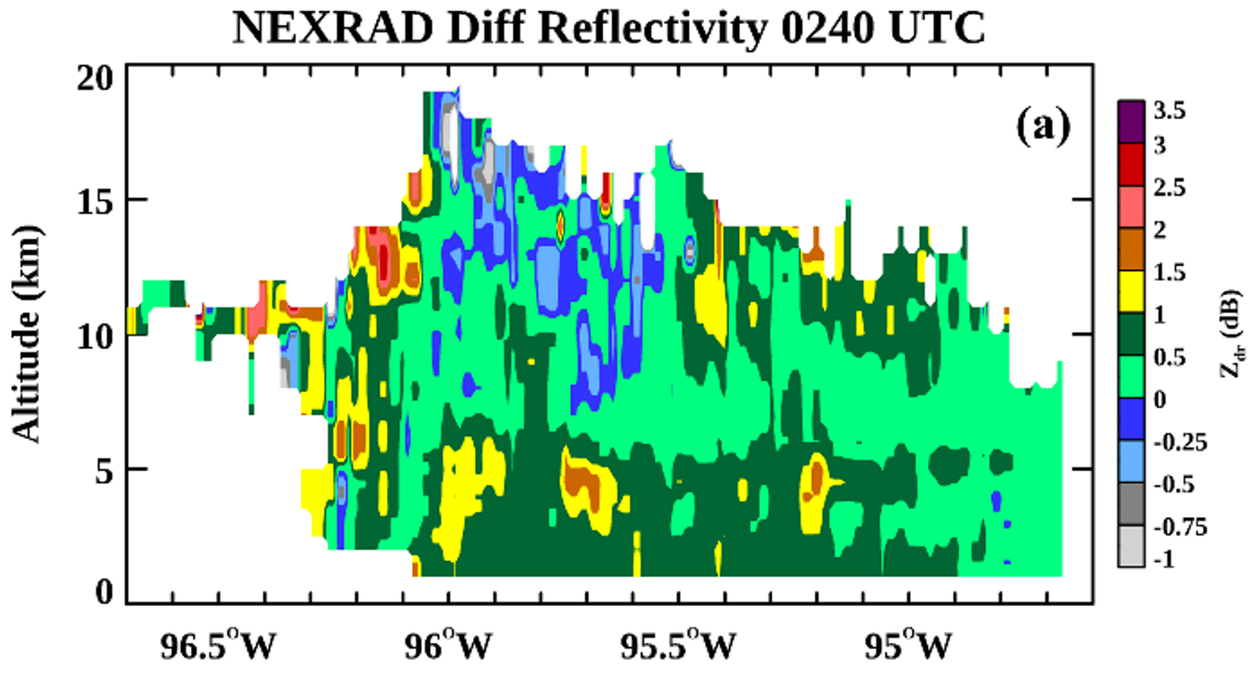
NEXRAD Diff Reflectivity 0240 UTC
(a)
Altitude (km)
20
15
10
5
0
96.5°W
96°W
95.5°W
95°W
3.5
3
2.5
2
1.5
1
0.5
0
-0.25
-0.5
-0.75
-1
Z_dr (dB)

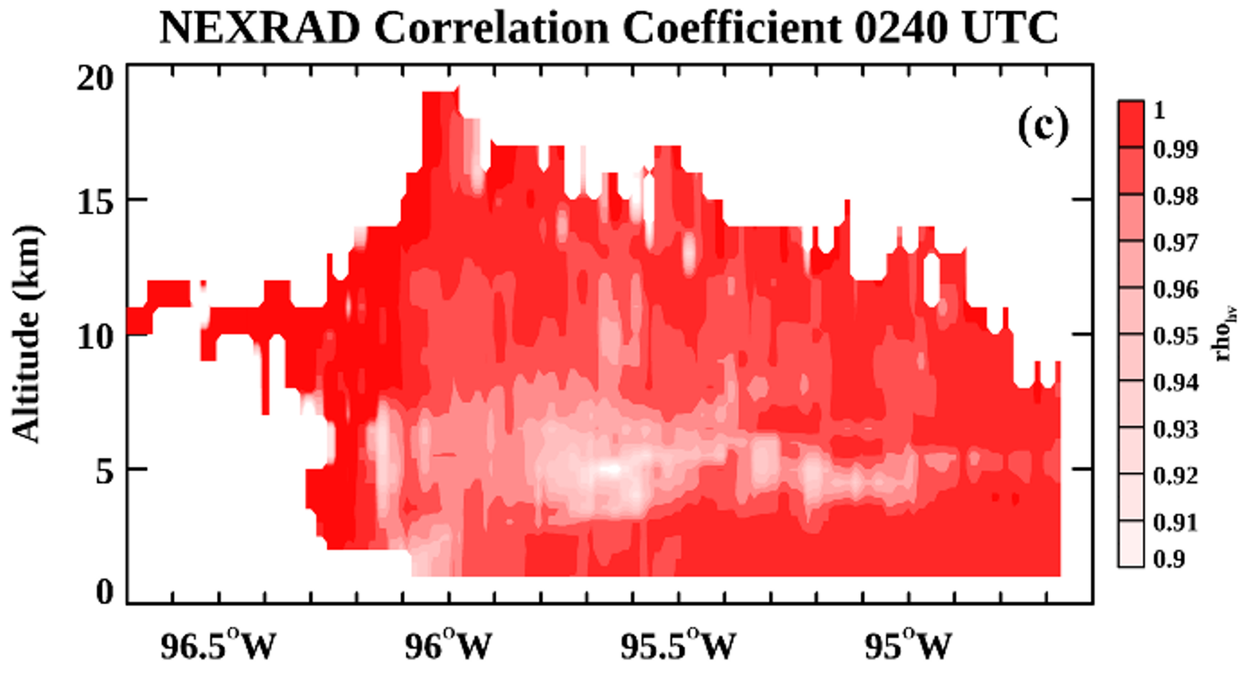
NEXRAD Correlation Coefficient 0240 UTC
(c)
Altitude (km)
20
15
10
5
0
96.5°W
96°W
95.5°W
95°W
1
0.99
0.98
0.97
0.96
0.95
0.94
0.93
0.92
0.91
0.9
rho_hv

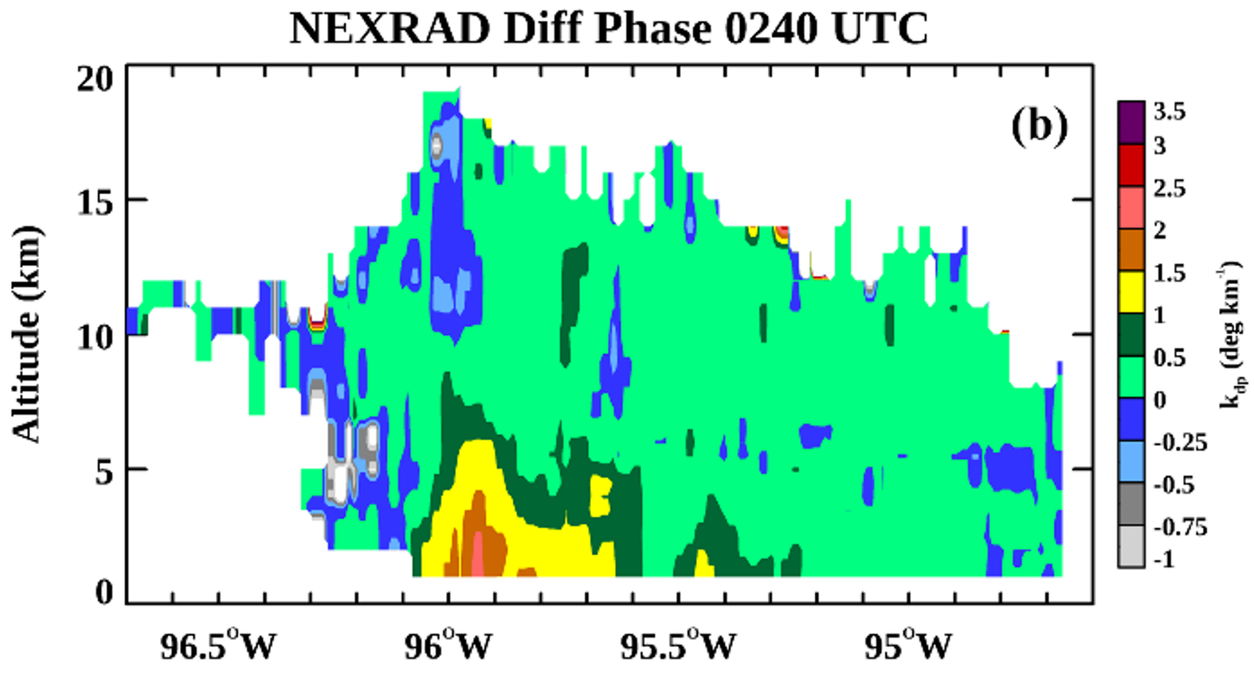
NEXRAD Diff Phase 0240 UTC
(b)
Altitude (km)
20
15
10
5
0
96.5°W
96°W
95.5°W
95°W
3.5
3
2.5
2
1.5
1
0.5
0
-0.25
-0.5
-0.75
-1
k_dp (deg km^-1)

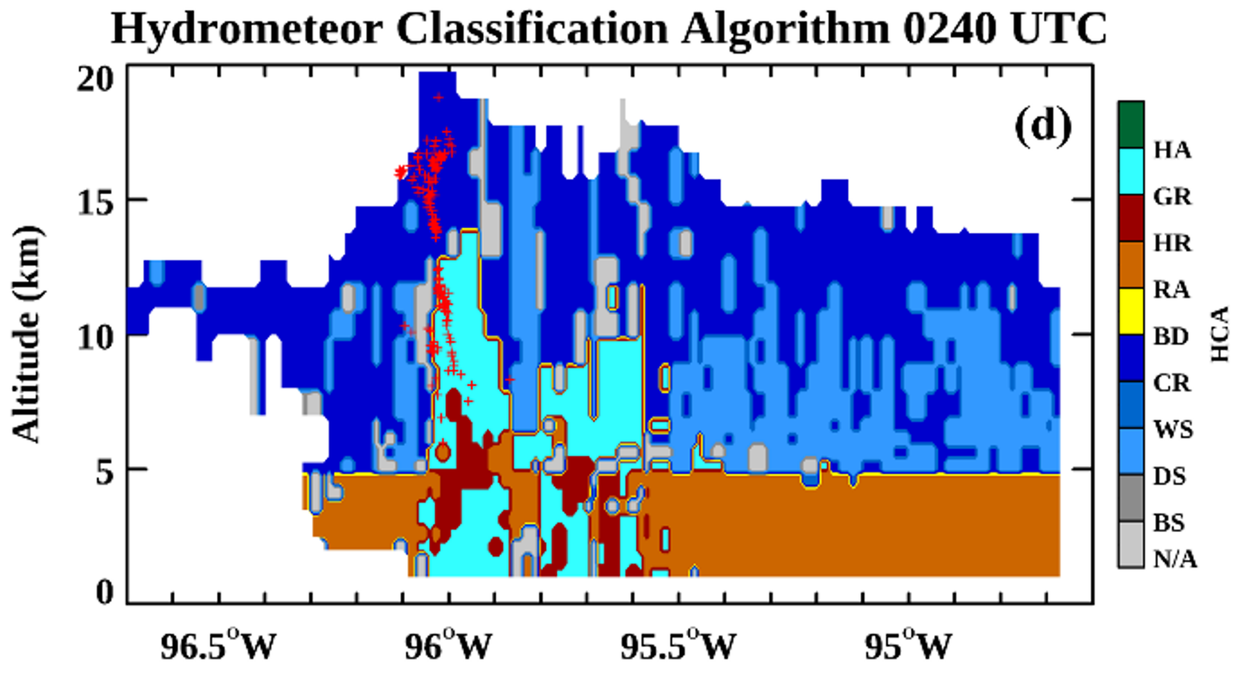
Hydrometeor Classification Algorithm 0240 UTC
(d)
Altitude (km)
20
15
10
5
0
96.5°W
96°W
95.5°W
95°W
HA
GR
HR
RA
BD
CR
WS
DS
BS
N/A
HCA

Figure 11.

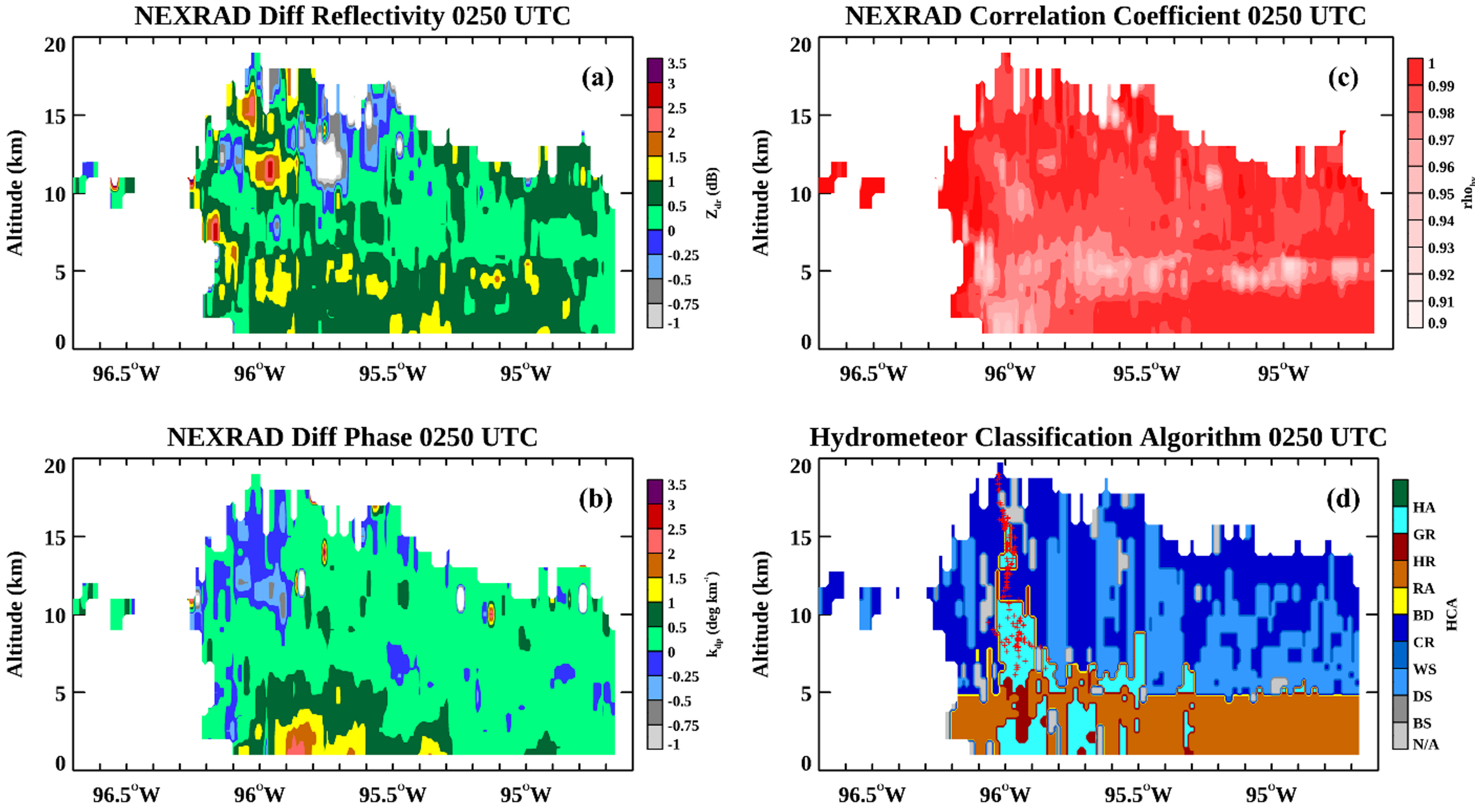
NEXRAD Diff Reflectivity 0250 UTC
(a)
Altitude (km)
20
15
10
5
0
96.5°W
96°W
95.5°W
95°W
3.5
3
2.5
2
1.5
1
0.5
0
-0.25
-0.5
-0.75
-1
Z_{dr} (dB)
NEXRAD Correlation Coefficient 0250 UTC
(c)
1
0.99
0.98
0.97
0.96
0.95
0.94
0.93
0.92
0.91
0.9
rho_{hv}
NEXRAD Diff Phase 0250 UTC
(b)
k_{dp} (deg km^{-1})
Hydrometeor Classification Algorithm 0250 UTC
(d)
HA
GR
HR
RA
BD
CR
WS
DS
BS
N/A
HCA

Figure 12.

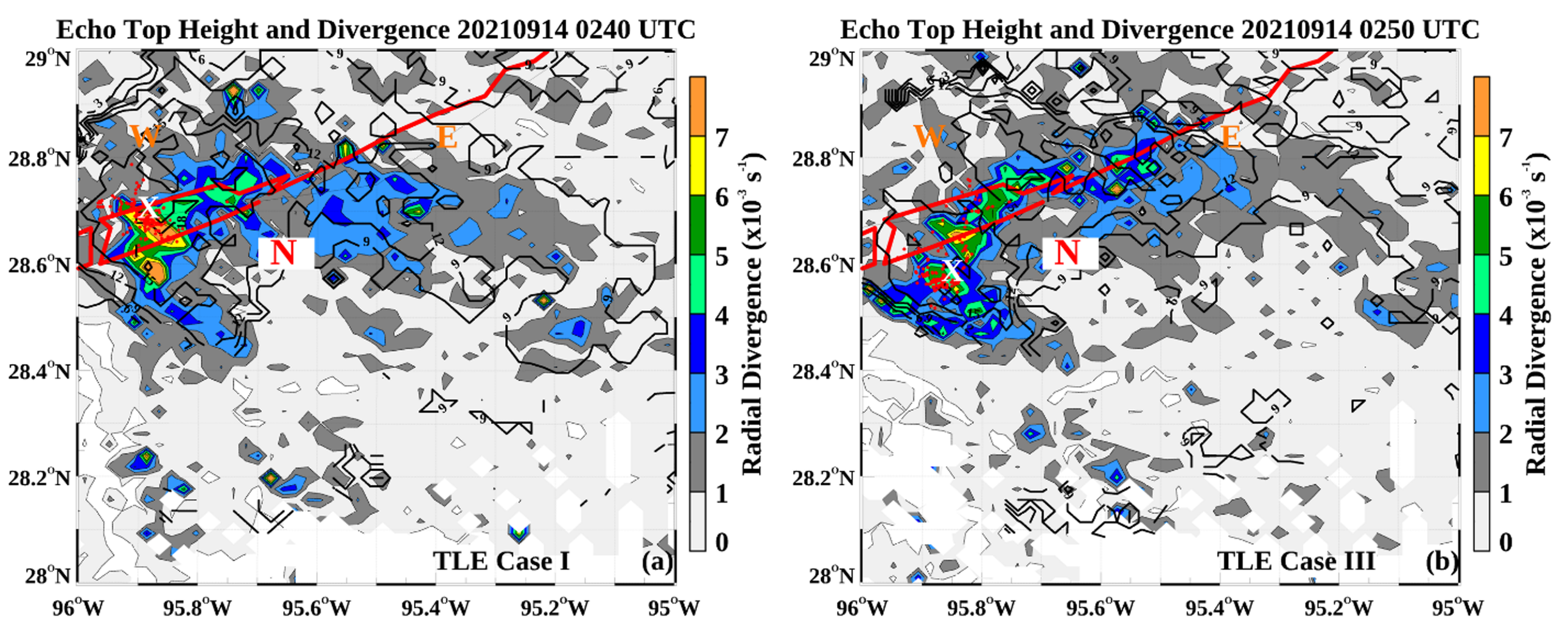
Echo Top Height and Divergence 20210914 0240 UTC
Echo Top Height and Divergence 20210914 0250 UTC
29°N
28.8°N
28.6°N
28.4°N
28.2°N
28°N
96°W
95.8°W
95.6°W
95.4°W
95.2°W
95°W
W
E
N
X
TLE Case I
(a)
TLE Case III
(b)
Radial Divergence (x10^{-3} s^{-1})
0
1
2
3
4
5
6
7